Modelling the Transport of Saharan Dust

James Richard Banks

Supervisors: Dr. Don Grainger, Dr. Martin Juckes

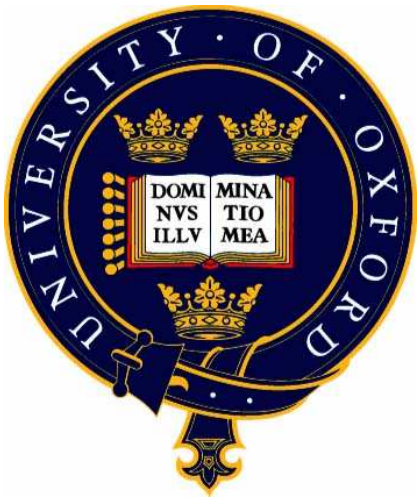

First year report

Atmospheric, Oceanic, and Planetary Physics
Department of Physics
University of Oxford

August 2007

Contents

Abstract

Tropospheric aerosols have a significant influence on climate and have been recognised by the Intergovernmental Panel on Climate Change as the biggest source of uncertainty in understanding future climate, yet the factors controlling their spatial distribution remain unclear. New observations from the UK ATSR instruments and the MODIS instrument (on NASA's Terra and Aqua satellites) provide global estimates of aerosol optical thickness and particle effective radius. This is significant progress on previously available measurements, but leaves open questions about aerosol sources, sinks, microphysical properties and the aerosol vertical distribution. In this study, a one-dimensional dust lifting model, using meteorological fields from ECMWF analyses, is used to compare predicted dust loading with observations. The model will be used to investigate the sensitivity of the predicted aerosol profiles to variations in model parameters.

This report describes the work that I have done over the past year into researching the background to dust transport and its detection by satellites, and describes the produced model. I begin (chapter 1) with the geographical background to dust sources and transport, and the significance of dust within the global climate system. I also review previous work carried out into modelling dust transport. I continue (chapter 2) by reviewing the satellite instruments used to detect the aerosol burden, using optical depth measurements. The produced model is described in chapter 3, including the physical basis for the method used, the operation of the model, and some simulated results output by the model. I conclude (chapter 4) by describing the further work that will be done to produce a more complete model.

I am grateful to my supervisors, Don Grainger and Martin Juckes, for all their help, advice, and time they have given me over the past year. The project is funded by the Natural Environment Research Council (NERC).

Chapter 1

Introduction

The radiative forcing of airborne aerosols is one of the most significant uncertainties in our understanding of climate change. Airborne aerosols have a number of different sources: soot pollution and biomass burning (anthropogenic), volcanic ash, and desert dust. The emission of desert dust is a purely natural occurrence (unlike pollution); however, human causes may amplify the production of airborne dust aerosol through overgrazing or deforestation, both of which can lead to desertification. The most obvious example of this is the Sahel region in Africa, which forms the southern boundary of the Sahara desert.

The Sahara desert itself is by far the largest source of desert dust in the world: it is the largest desert in terms of area, it has the strongest source in the world (the Bodélé Depression in Chad), and emits a total mass of 630-710 Tg of dust per year according to D'Almeida (1986), or 1400 Tg per year according to McKendry et al. (2007). This compares to the estimated global emission of 1000-3000 Tg per year (Engelstaedter et al., 2006).

Airborne desert dust has several effects on the global environment. Once aloft, aerosols increase the optical depth, altering the heat budget of the atmosphere (optical depth derived from radiance is the quantity that satellites measure in order to infer the presence of aerosols). Aerosols scatter and absorb solar and out-going thermal radiation, which affects the climate (Engelstaedter et al., 2006). On deposition, desert dust can act as a fertiliser, for example in the Amazon (Swap et al., 1992), where the quantities of sodium, potassium, chlorine, nitrates, sulphates, and phosphates are enriched by Saharan dust. This is an essential part of the nutrient balance which makes the Amazon rainforest so fertile. Dust deposited into the oceans/seas provides iron, which enhances the production of chlorophyll (Mahowald et al., 2005): this has important implications for the CO_2 budget, since increased productivity will cause a decrease of CO_2 in the atmosphere. Another consequence of airborne desert dust is the weakening of tropical storms (Engelstaedter et al., 2006). Human activity is influenced by desert dust as well, since aerosols can spread fungi and bacteria (causing disease), the dust itself can worsen respiratory problems, and the reduced visibility has been responsible for several aviation disasters in North Africa.

1.1 Sources of desert dust

1.1.1 Saharan sources

For the purposes of this study, the 'Sahara region' encompasses not just the Sahara desert itself, which occupies most of North Africa, but also extends into the Sahel (which forms the southern boundary of the Sahara; the dividing line between the Sahara and the Sahel is not a distinct boundary, it changes seasonally), the Arabian peninsula, and the Middle East. The longitude and latitude coordinates which form the bounds of this region are: 17.8 °W, 37.4 °N, 59.7 °E, and 7.9 °N. The Canary Islands and the Atlantic form the western boundary, the Mediterranean, Syria and Iraq form the northern boundary, Oman forms the eastern boundary, and the countries of the Sahel (Senegal, Mali, Burkina Faso, Niger, Chad, Sudan, and Somalia) form the southern boundary. Arabia and the Middle East are a significant source of dust, and the Red Sea which divides it from the Sahara is narrow enough that the Saharan and Arabian deserts can be treated as one.

There are a large number of distinct sources in the Sahara region, too many to be described here. Below are described some of the most significant and interesting sources; for a more complete picture, consult Prospero et al. (2002) or Goudie and Middleton (2006). Aside from the regions descibed below, there are active source regions in Tunisia, northern Algeria, Libya, Egypt, Sudan, the Ethiopian Rift Valley, and Djibouti.

Through much of the following sections the strength of dust emissions will be referred to using the TOMS (Total Ozone Mapping Spectrometer) aerosol index (TOMS AI), commonly used to refer to the geographical distributions of dust sources. According to Ginoux and Torres (2003), the TOMS AI is defined as:

$$AI = -100\Big[\log\left(\frac{I^m_{340}}{I^m_{380}}\right) - \log\left(\frac{I^c_{340}}{I^c_{380}}\right)\Big] \tag{1.1}$$

I^m_{340} is the measured backscattering radiance at 340 nm, and I^c_{340} is the radiance using a radiative transfer model which assumes a pure Rayleigh atmosphere. It is therefore a measure of how much the backscattered radiance is affected by the aerosol present in the atmosphere.

The Bodélé depression

TOMS and MODIS data indicate a significant source of desert dust coming out of Chad (Engelstaedter et al., 2006) in the region of the Bodélé depression (16 °-18 °N and 15 °-19 °E), with yearly mean AI (aerosol index) values exceeding 3.0. Bodélé is the best example of a *preferential source region*, or *hot spot*, from where a concentrated plume of dust is emitted. This appears to be the most active dust producing region in the world, and is one of the most significant suppliers of mineral dust to the Amazon rainforest (Koren et al., 2006). Also, unlike most other dust sources in the world, Bodélé is active year-round, even in the autumn/winter months of October-December when the rest of the Sahara is inactive. The source is particularly strong between April and June, when the TOMS AI is greater than 1.9 on 75% of the days (Goudie and Middleton, 2006) (p.92).

Grini et al. (2005) identifies several important factors which produce a hot spot: (1) high wind speeds, (2) low threshold wind velocity, (3) lack of crusting, (4) high particle availability. Lack of crusting is important because crusted surfaces, being very hard, are very resistant to wind erosion. (Goudie and Middleton, 2006) (p.38) refer to *stone/desert pavements*, similar to *duricrusts* (hardened surface crusts found in many arid regions),

Figure 1.1: Map of North Africa. (Image courtesy of www.mytravelguide.com/travel-tools/maps/North-Africa-map.php, accessed 31/7/2007).

which are also widespread in arid regions and consist of an armour of coarse particles covering a substantial amount of fines, probably caused by dust deposition from the atmosphere. If the crust is disturbed or cracked, for example due to human activity such as road building, then these areas can become local sources of dust. In general, what we are looking for in a source region is a substantial quantity of exposed fine particles. This is usually due to the presence of silt particles, so we are looking for areas which are fed by streams (to carry alluvium), but which are sufficiently arid that there is very little vegetation. Moreover, soil moisture (Mahowald et al., 2005) strengthens the cohesion forces between the soil grains (which hinders erosion), so these streams should be ephemeral, being dry during most of the year.

The Bodélé depression is such a significant source of dust due to three main factors: it is situated in a region with reliably strong winds, it contains a significant quantity of fine particles, and is downwind of a region which produces saltating coarse particles. The Bodélé depression is a dried lake bed, and is associated with Lake Chad. The region is very dry, with very low rainfall (average annual rainfall of about 17 mm (Goudie and Middleton, 2006) (p.84), which means both that there is very little vegetation (which hinders dust emission) and a low possibility of wet deposition of dust particles. Meanwhile, streams from the wetter Tibesti massif to the north supply the depression with silty alluvium. According to Mahowald et al. (2005), precipitation must be low in the dust source so that the soils are free to erode, while greater precipitation in adjacent highlands increases the availability of finer particles. As a result of this, the Bodélé contains a significant quantity of erodible sediment (Washington et al., 2006b): this means that the soil particles dominating the Bodélé are susceptible to being lifted from the surface, since the particles are so fine. Moreover, as it is surrounded by Saharan desert, the Bodélé gets bombarded by coarser particles saltating down into the depression: this is significant since it is primarily the influence of saltating particles which ejects dust into the atmosphere.

The winds in this region tend to coincide on the Bodélé depression, since to the north and east of Bodélé are situated the Tibesti and the Ennedi mountain ranges. The effect of this is that north-easterly winds are channelled and focused between the two mountain ranges, downslope and at low altitude, onto the Bodélé depression, so that the anomalously strong down-slope flow is statistically linked to the enhanced wind erosivity in the depression (Washington et al., 2006b). This characteristic wind is known as the Bodélé Low Level Jet (LLJ). The LLJ drives the saltation process of coarser particles which initiates the emission of the finer dust particles up into the atmosphere.

West Africa

West Africa is the other main source of airborne dust in the Sahara, though the main emitting region here has a much wider area than does the Bodélé depression. According to Prospero et al. (2002) there is a large active area from 17 °-18 °N, 8 °-10 °W to the ENE to 26 °N along the meridian, covering large parts of Mali, Mauritania, and southern Algeria. According to Goudie and Middleton (2006) (p.86), the region is an area of low relief bounded to the north and east by highlands. Highlands may not be major dust source regions, but ephemeral wadis draining from them transport silt-rich alluvium. This is comparable to the effect of the Tibesti massif on Bodélé. Niger is also quite active. Though the average dust emission from west Africa is lower than from Bodélé, the extent of the west African source region means that this area emits a comparable quantity of dust into the atmosphere. West Africa emits dust more seasonally than does Bodélé, with very low emissions over the winter, from October to March. Between April and September,

the TOMS AI is greater than 1.9 on 75% of the days (Goudie and Middleton, 2006) (p.92).

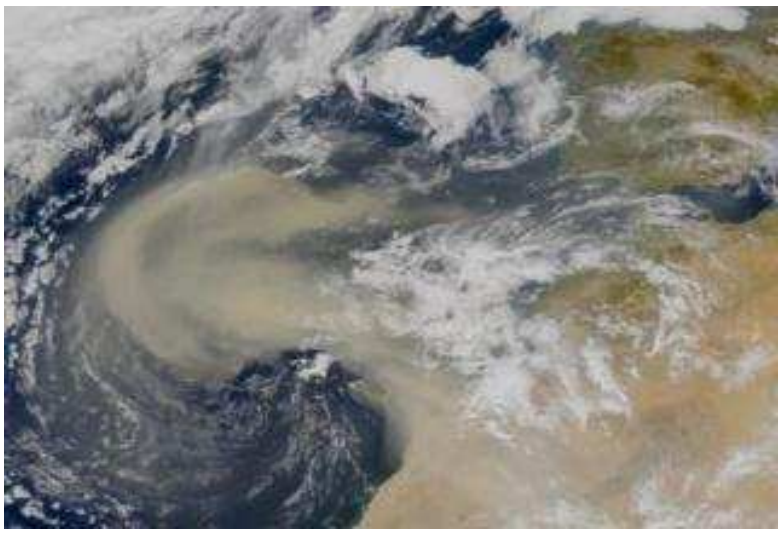

Figure 1.2: Dust plume in the Atlantic off the Western Sahara (SeaWiFs, 26/2/2000, image courtesy of NASA).

The Middle East

The Middle Eastern desert region covers most of the Arabian peninsula, Iraq, eastern Syria, Jordan, and the Negev desert in southern Israel. While most of Arabia up into Iraq and Syria is sandy desert, the hills running up Arabia's Red Sea coast, through western Jordan and into south-western Syria, hinder dust emission because of their rough topography. Goudie and Middleton (2006) (p.112) show that the area with the highest dust storm activity in the Middle East is a swathe of land in eastern Saudi Arabia (just to the east of Riyadh), stretching from the Persian Gulf near Bahrain down to the Rub Al Khali (the 'Empty Quarter') desert in the south. Dust storm activity occurs all-year round. This region is predominantly flat and featureless, with relatively fine particles, bordered by a sand sea, the Ad Dahna, to trigger emission through saltation. Oman is also a significant source.

In Iraq, the focus of dust activity appears to be in the Tigris and Euphrates Basin ('Mesopotamia'), rather than in the substantial deserts to the west and south of the country. This is perhaps not surprising, since the basin is a source of fines, fed by the two major rivers running through the heart of the country. A particularly strong source is at the mouth of the river system (flowing into the Persian Gulf), where there are 43 (Prospero et al., 2002) dust storms per year on average. It is possible that the draining of the marshlands of southern Iraq after the first Gulf War has increased the frequency of the dust storms.

Figure 1.3: Dust plume being blown off Arabia and over the Persian Gulf (MODIS, April 2003, image courtesy of NASA).

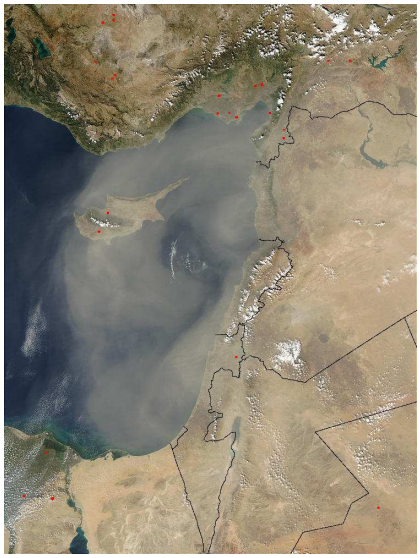

Figure 1.4: Dust storm emanating from the Middle East, travelling westwards over the Mediterranean. Image taken by MODIS on 19/10/2002, image courtesy of NASA).

1.1.2 Non-Saharan sources

China and Central Asia

China is one of the largest sources of dust in the world: one estimate (Goudie and Middleton, 2006) (p.137) puts the total annual emission of dust from China at ∼800 Tg, as much

as half of the global emission. Though the current study is focusing on the Sahara region, it is important to note that it is not the only major source of dust. The main source of desert dust in China is the Taklamakan desert in the west of the country, Xinjiang province. The Taklamakan is contained within the Tarim Pendi basin, which is bounded by the mountains of the Himalaya to the south, the Hindu Kush to the west, and the Tien Shan to the north (on the border between China and Kyrgyzstan): its range is 75 °-90 °E, 36 °-40 °N. The mean TOMS AI value at the centre of the Taklamakan exceeds 11.

Another Chinese source is the Gobi desert, which despite being a stony desert (which hinders dust emission) is actually a strong source of airborne aerosol. Despite the fact that the Taklamakan appears to be a more significant source from the TOMS data, (Goudie and Middleton, 2006) (p.137) report that the Gobi may be the strongest source in the region, with emission fluxes up to 5000 μg m^{-2} s^{-1}. The difference between the two deserts is that the Taklamakan is a more persistent emitter of dust, whereas the Gobi emits fewer, but more intense, dust storms. These tend to occur in winter, when strong storms blow in from Siberia.

The Central Asian countries, especially Kazakhstan, Uzbekistan, and Turkmenistan, are another important source of dust. The region has a number of salt lakes, a typical source of airborne dust, and the Aral Sea (between Kazakhstan and Uzbekistan) is increasingly becoming a source itself. Soviet damming of the Amu Darya river (which supplies the Aral Sea) has diverted water away from the Aral Sea for irrigation, so over the last few decades the sea has been shrinking, as have associated lakes and wetlands. This has exposed the sediments of the lake bed, fine particles which are susceptible to lifting. A corresponding increase in dust storm frequency has therefore been observed in Central Asia: at the Chabankazgan (Goudie and Middleton, 2006) (p.183) station in Uzbekistan, the annual frequency has risen from 18.1 in the 1950s to 44.5 in the 1970s. This has had serious implications for the environment, and the health of the people living in the region, as far away as Turkmenistan.

Other sources

In southern Africa, the Kalahari desert contains two distinct sources of desert dust. In Botswana there is the Makgadikgadi Depression (21 °S, 26 °E), which is usually covered by shallow pools, sandy clays, and islands of grass (Prospero et al., 2002). The maximum of dust activity tends to be between August and October, outside the rainy season, when the depression is flooded. In Namibia there is the Etosha Pan (18 °S, 16 °E), a flat salt pan, and is perhaps indicative of the effects of human land use, since indigenous peoples were moved into the region.

South and western Asia contains a number of dust sources: in Iran there is the Dasht-e Kavir desert (Prospero et al., 2002) to the east of Tehran; there is the Seistan Basin in the Dasht-i-Margo on the border with Pakistan and Afghanistan; and there is the Makran coast, running from south-east Iran into Pakistan. In Pakistan, as well as these two sources, large areas of central Pakistan emit, as does the Indus delta region near Karachi. Meanwhile the Ganges plain in India is shown by TOMS (Goudie and Middleton, 2006) (p.122) to be a heightened source region compared to the rest of India.

Though North America is generally a net importer of airborne dust, there are source areas. These are concentrated in the Great Plains, in Texas, Oklahoma, Colorado, Kansas, and Nebraska, with a smaller source region up in North Dakota into southern Saskatchewan (Canada). There is another source region to the west in the deserts of Arizona, Nevada, and California. Meanwhile, large areas of Mexico are also suitable for

dust lifting, since the country has an arid climate.

In South America, there are two main source areas, the Altiplano region in Peru, Bolivia, and Chile, and the Patagonia region in Argentina. Within the Bolivian Altiplano is the Salar de Uyuni, a closed basin containing salt flats similar in size to other major dust producing depressions such as Bodélé and the Taklamakan.

Australia contains one major source of dust within its large and arid interior, the Great Artesian Basin/Lake Eyre, in South Australia. Knight et al. (1995) report a major dust event from 1987 which removed between 1.9 and 3.4 Tg of dust from the Simpson Desert out of Australia over the Tasman Sea towards New Zealand. They estimate that the Simpson Desert loses an average of 107-122 tonnes km^{-2} yr^{-1}, substantially larger than the 32-45 tonnes km^{-2} yr^{-1} of sediment lost by Australian rivers.

1.2 Trajectories of Saharan desert dust

There are three principal routes for Saharan dust plumes: the Atlantic, the Mediterranean, and across Arabia and the Middle East to Asia.

1.2.1 The Atlantic and the Americas

Western trajectories transport Saharan dust across the Atlantic, principally to South America but also to the Caribbean and North America. Goudie and Middleton (2006) (p.95) report that 30-50 % of the desert dust output from the Sahara passes over the Atlantic. Estimates using MODIS data (Kaufman et al., 2005) suggest that 240 $\pm$ 80 Tg of dust per year are transported ove the Atlantic. Useful places to measure Saharan dust transport over the Atlantic are on islands, such as Barbados and Sal Island (in the Cape Verde Islands) (Ellis and Merrill, 1995), which indicate the transport of dust in oceanic conditions. The Cape Verde Islands are a particularly useful location since they are so close to the coast of West Africa, and can be used to estimate the total emission from the western Sahara into the Atlantic.

A dust plume takes about 5-7 days to travel from West Africa to the Caribbean (Middleton and Goudie, 2001), with the greatest frequency of dust events to that region of the Atlantic occurring during the summer, especially July and August. Measurements at Cayenne (French Guiana) indicate that the strongest dust activity is in March. The West African sources (Mali, Mauritania, Algeria, and Morocco) are the main source regions for the North Atlantic, while Koren et al. (2006) suggest that the Bodélé depression is a major source to the Amazon Basin, since it releases 56 % of the total annual burden of airborne desert dust, and in winter is responsible for >40 % of dust optical depth over the Amazon.

1.2.2 The Mediterranean and Europe

Northern trajectories transport Saharan dust over the Mediterranean to Europe, and can be quite frequent: in 1999, on 100 % (Middleton and Goudie, 2001) of the days in June and August the TOMS AI value exceeded 1.9 over the Mediterranean Basin. The summer is the most active season for dust events, due to the Sahara, which accounts for 80-120 $\times 10^6$ tons per year (D'Almeida, 1986) over Europe. The sources for these events tend to

be from West Africa, in central and southern Algeria, Morocco, Tunisia, and Libya. This trajectory can supply dust to northern Europe, to Britain via mid-tropospheric winds in the Bay of Biscay (Middleton and Goudie, 2001), and as far north as Scandinavia. Wet deposition is a common form of deposition over Europe.

Saharan dust also has an impact on the mineralogy of the Mediterranean: Guerzoni et al. (1997) report that deep-sea sediments from the Tyrrhenian and Adriatic seas have similar clay mineral signatures to Saharan dust. This is not true in the eastern Mediterranean, where smectites predominate, indicating output from the Nile; the presence of the Aswan Dam should reduce the proportion of smectites and increase the proportion of Saharan dust in the sediments in future.

1.2.3 The Middle East, Asia, and the Pacific

Dust transported over the Middle East comes not just from the Middle East itself but also from the Sahara, from as far west as Algeria (Goudie and Middleton, 2006) (p.114), crossing the southern Mediterranean and the northern Sahara to Cyprus, Turkey, Israel, Jordan, Lebanon, Syria, Iraq, and across the Arabian peninsula. TOMS data from March 2002 show a storm developing in Libya and Egypt on the 18th, strengthening over the Levant on the 19th, and passing over Iraq through to north-eastern Iran on the 20th. Sudan's Red Sea coast is another source of dust transported across the Red Sea to the Middle East, since the region contains two large sources of silt, the Tokar delta, and the ephemeral Baraka river.

There are indications that Saharan dust can travel even further east than Asia. McKendry et al. (2007) report a dust event in British Columbia, Canada, on 13-14 March 2005, generated in North Africa between the 28th February and the 3rd March. This trajectory would have taken the dust over the Middle East, across Asia, and across the northern Pacific. Lidar and sunphotometer measurements in British Columbia showed a subtle increase in optical depth, observing an optical depth (at 500 nm) of 0.1 due to the dust. Global chemical models indicated that the observed dust over the Sahara would be transported eastwards over the Pacific, and the unusually low dust activity over China (generally the source of the greater proportion of dust over the Pacific) suggested that the observed dust over Canada was from the Sahara.

1.3 Specific Science Questions

The dust transport model that is the subject of this report is to be used to pursue several science questions. The processes in question can be broadly separated into two types: *natural* and *anthropogenic*. An example of a natural process for which more study is desirable is the effect of the Bodélé Depression on the global atmosphere, and in particular its effect on the fertility of the Amazon rainforest after deposition. A similar question is how much dust is deposited into the seas and oceans, and its effect on marine life.

In the Sahara region, the most important anthropogenic process to be studied is the effect of desertification in the Sahel. The Sahel is potentially a very large source of dust, and is recognised as a significant contributor to the atmospheric dust load (Tegen and Fung, 1995). Moreover, since the Sahel is a recently fertile region, which has been recently eroded (by, for example, agricultural practices), it is a source of fines, such as silt and clay.

This is in contrast to older deserts where the soil is likely to be coarser, since the fines will generally have been already blown out: therefore the Sahel and other such regions can be a larger source of atmospheric aerosol than more established deserts. Due to the scale of the Sahel, modelling processes within this region will require the model to be thousands of kilometres across.

Desertification of lakes is another potential source of dust to be studied. The best example of this is the Aral Sea. As with the Sahel, exposure of the lake bed makes available a new and potentially significant source of fine dust particles for lifting into the atmosphere. Drying of lake beds is on a smaller scale than the desertification of the Sahel, so the area of interest is likely only to be of the order of a few hundreds of kilometres. However, the resolution required would be finer than for modelling the Sahel, since the scale of the drying areas of the sea is of the order of tens of kilometres only.

A much more localised dust source that is worthy of further attention is the effect of road building in established desert areas. As mentioned in section 1.1.1, many desert regions are covered by duricrusts and desert pavements, which are a crust of tightly packed coarse materials, which are not susceptible to lifting, overlaid on top of a quantity of fines. If this surface is cracked, for example by roads or other such human activity, then these fines can be exposed and become a locally strong source of dust. Within the context of this model, small length and time scales would be needed to model this process, since the width of a road is only of the order of metres (though the length of the stretch of road of interest may be of the order of kilometres).

1.4 Dust Transport Models

Previous work has been carried out into dust transport models, on varying scales. Some models, such as the Global Ozone Chemistry Aerosol Radiation and Transport (GOCART) and the Dust Entrainment And Deposition (DEAD) models, operate on a global scale, simulating dust emission from sources, horizontal and vertical transport, and deposition: these have been used to predict the distribution of the annual mean dust loadings, optical depths, and dust deposition. This is in contrast to the current model, which is more regional in scope. Other models are more specific, tracking the trajectories of a particular plume of dust, for example, over the Atlantic, or across Asia and the Pacific. Summarised below are some examples of these.

1.4.1 The model of *Tegen & Fung*, 1994

An early global 3D model of dust transport was presented by Tegen and Fung (1994) in 1994, simulated using the tracer transport model of the Goddard Institute for Space Studies. The model is driven by assimilated data from the European Centre for Medium Range Weather Forecasting (ECMWF) with a $1.125 \times 1.125^\circ$ grid, and a $1 \times 1^\circ$ soil data set of soil types.

Four particle size classes are used: clay, with radii between 0.5 and 1 μm and a constant size distribution $dM/dlogr$ (where M is the mass of particles of radius r); small silt, between 1 and 10 μm and constant dM/dr; large silt, between 10 and 25 μm and constant dM/dr; and sand, between 25 and 50 μm and constant dM/dr. The emission

flux of uplifted dust is given by:

$$q_{\mathrm{a}} = C(u - u_{\mathrm{tr}})u^2 \tag{1.2}$$

The surface wind speed is u, u_{tr} is the threshold wind velocity (the minimum wind velocity that will mobilise dust particles) set constant at 6.5 ms^{-1}, and C is a dimensional factor constant for all size classes, determined a posteriori. As such, the model is an example of a *bulk mobilisation scheme* (Zender et al., 2003), since this model mobilises dust depending on the third or fourth power of the wind speed and imposes an empirical size distribution upon the emitted dust. That $\mathrm{u_{tr}}$ is constant is a weakness in the model, since the threshold velocity varies significantly with particle size, especially for sub-micron particles.

Dry deposition by gravitational settling is determined using Stokes' law:

$$v_{\mathrm{stk}} = \frac{2g\rho r^2}{9\nu} \tag{1.3}$$

Where ρ is the particle density, ν is the air viscosity and g is gravitational acceleration. The dry turbulent diffusion to the surface is:

$$v_{\mathrm{d}} = uC_{\mathrm{D}} \tag{1.4}$$

Where u is the surface wind speed and C_{D} is the drag coefficient. Wet deposition is modelled using a scavenging ratio, Z, defined by:

$$Z = C_{\mathrm{rain}}/C_{\mathrm{air}} \tag{1.5}$$

C_{rain} is the concentration in rain in grams of dust per kilogram of rainwater and C_{air} is the aerosol concentration in air in grams of dust per kilogram of air. Wet deposition determines the atmospheric lifetime for clay particles, while for silt and sand particles dry deposition predominates.

The model results suggest that the global dust emission is 3000 Tg year^{-1}, from 390 Tg year^{-1} clay, 1960 Tg year^{-1} silt, and 650 Tg year^{-1} sand. Meanwhile, the maximum seasonal mean of the optical depth is found to be 0.5. However, since the model's resolution is quite crude (a $4{\times}5\,^{\circ}$ grid is used by the GCM for advection) it has been surpassed by the more precise GOCART and DEAD models.

1.4.2 The GOCART model

The Global Ozone Chemistry Aerosol Radiation and Transport (GOCART) model (Ginoux et al., 2001, 2004) has been produced at the Georgia Institute of Technology and at the NASA Goddard Space Flight Center. It is a global model, and is used to measure not just the transport of mineral dust, but also other aerosols and trace gases, such as sea salt, sulphates (Chin et al., 2000), carbon monoxide (CO) (Allen et al., 1996), and ozone.

The model uses assimilated meteorological data (horizontal winds, surface pressure, temperature, etc.) from the Goddard Earth Observing System Data Assimilation System (GEOS DAS) on a $2\,^{\circ}$ latitude by $2.5\,^{\circ}$ longitude grid, with 20-40 height layers. It calculates, using the method of operator-splitting, seven aerosol processes: emission from the surface; chemistry (aerosol microphysics, such as aerosol-cloud interactions); advection, using a flux-form semi-Lagrangian transport scheme (Lin and Rood, 1996); diffusion; convection; dry deposition; wet deposition. These processes are calculated for four size bins: 0.1-1 (0.75), 1-2 (1.5), 2-3 (2.5), and 3-6 (4.5) μm radius, with the numbers in brackets

representing the average radius. The fall velocities within these bins are assumed to be constant across the range. Within each bin the size distribution $dM/dlnr$ is constant. Particles larger than this have very short lifetimes (close to the surface in saltation) and are ignored by the model. The time step is 20 minutes, and the wind fields are linearly interpolated to every time step, from the instantaneous values at every six hours. The model is initialised with near-zero mass, and is spun-up for 1 month (Ginoux et al., 2001).

Emission is simulated using the following empirical formulation:

$$F_{\mathrm{p}} = \begin{cases} C s_{\mathrm{p}} u_{10\mathrm{m}}^2 (u_{10\mathrm{m}} - u_{\mathrm{tp}}) & \text{if } u_{10\mathrm{m}} > u_{\mathrm{tp}} \\ 0 & \text{otherwise} \end{cases} \tag{1.6}$$

Where C is a dimensional factor, and the source fraction values s_{p} are 0.1 for the radius class 0.1-1 μm and 0.3 for the remaining 3 classes. The threshold velocity is u_{tp}; when surface wetness is taken into account, the threshold velocity is:

$$u_{\mathrm{twp}} = \begin{cases} u_{\mathrm{tp}}(1.2 + 0.2 \log w) & \text{if } w < 0.5 \\ \infty & \text{otherwise} \end{cases} \tag{1.7}$$

The surface wetness is w, u_{tp} is the threshold wind velocity, similar to u_{tr} in the the model by Tegen and Fung (1994); however, for the model that is the subject of this report, w has been assumed to be 0.1, due to a lack of data pertaining to w; therefore the threshold velocity u_{twp} simply reduces to u_{tp}. For arid regions w ranges from 0.001 to 0.1, after precipitation w is typically 0.5, while over water, w is 1: 0.1 is therefore a reasonable approximation for w over the Sahara region. For deposition, the GOCART model modifies the turbulent diffusion settling term v_{d} by taking into account the surface wetness if the surface wind speed $u_{10\mathrm{m}}$ exceeds the threshold velocity u_{tp}.

$$v_{\mathrm{d}}^* = \begin{cases} v_{\mathrm{d}}(w + (1-w)\exp[-(u_{10\mathrm{m}} - u_{\mathrm{tp}})]) & \text{if } u_{10\mathrm{m}} > u_{\mathrm{tp}} \\ v_{\mathrm{d}} & \text{otherwise} \end{cases} \tag{1.8}$$

GOCART uses a Stokes' settling velocity term v_{stk}.

The results from the model presented here are taken from Ginoux et al. (2004). The model was run using data from 1981-1996, and predicts a maximum annual emission of airborne dust of 2400 Tg, calculated for 1988, and a minimum of 1950 Tg in 1996. Sixty-five percent of these emissions are from North Africa, 25% are from Asia. That North Africa is the main emitter of mineral dust is expected, and they found that in winter the Bodélé depression is the major dust source. Ninety percent of the dust deposition occurs due to dry deposition, and this has significant regional variations. Meanwhile, North America is shown to be a net sink of dust, taking in 30 Tg year^{-1} more dust than it emits: North African sources of dust are the major contributors to North American deposition.

1.4.3 The DEAD model

The Dust Entrainment And Deposition (DEAD) model (Zender et al., 2003) has been produced at the University of California, and has been used to simulate global atmospheric dust distributions during the 1990s. Unlike the GOCART model, the DEAD model is focused exclusively on modelling the transport of mineral dust, though it is a component of a larger chemical model, the Model for Atmospheric Chemistry and Transport (MATCH). The model is driven by National Center for Environmental Prediction (NCEP) analysed meteorology.

Like the GOCART model, the DEAD model takes into account the microphysics of the soil (ie. the effect of particle sizes, soil moisture, and vegetation cover on the threshold velocity, u_{tp}) when calculating the emission from the surface. Saltation and sandblasting are assumed to be the causes of emission, and it assumed that the vertical emission flux of dust F_{d} is directly proportional to the total saltating horizontal mass flux Q_{s}:

$$F_{\mathrm{d}} = \alpha Q_{\mathrm{s}} \tag{1.9}$$

α is the sandblasting mass efficiency and is dependent on the mass fraction of clay, M_{clay}:

$$\alpha = 100 \exp\left[(13.4 M_{\mathrm{clay}} - 6)\ln 10\right] \tag{1.10}$$

Q_{s} is dependent on the air density ρ, the wind friction velocity u_*, and on u_{tp}.

$$Q_{\mathrm{s}} = \frac{2.61 \rho u_*^3}{g}\left(1 + \frac{u_{\mathrm{tp}}}{u_*}\right)\left(1 - \frac{u_{\mathrm{tp}}^2}{u_*^2}\right) \tag{1.11}$$

The model contains three deposition processes: gravitational settling, turbulent mixout, and wet deposition. A turbulent deposition velocity v_{t} is defined with respect to the gravitational settling velocity v_{g}, the aerodynamic resistance through the constant flux layer r_{a}, and the quasi-laminar layer resistance r_{b}, which depends on the particle's microphysical characteristics.

$$v_{\mathrm{t}} = \frac{1}{r_{\mathrm{a}} + r_{\mathrm{b}} + r_{\mathrm{a}} r_{\mathrm{b}} v_{\mathrm{g}}} \tag{1.12}$$

Meanwhile wet deposition is modelled by defining the grid cell aerosol mass path, M_{p} (kg m^{-2}), the normalised scavenging coefficients Λ_{M}, the rate of interaction with the scavenging droplets, P_{M} (kg m^{-2} s^{-1}), and the horizontal fraction of the grid cell over which the scavenging process occurs, A.

$$\frac{dM_{\mathrm{p}}}{dt} = A P_{\mathrm{M}} \Lambda_{\mathrm{M}} M_{\mathrm{p}} \tag{1.13}$$

The model assumes that each particle size bin is discrete and non-interacting with the other size bins. Each bin has an independent sub-grid size distribution, and this sub-bin distribution is time-invariant. The distribution is modelled by a trimodal lognormal probability density function (PDF), which depends on the number median diameter D_{n}, mass median diameter D_ν, geometric standard deviation σ_{g}, and the mass fraction M of each mode. The values used for the source function are given in table 1 of Zender et al. (2003).

The model predicts an average annual emission during the 1990s of 1490±160 Tg, rather less than the GOCART prediction, with Africa providing 980 Tg yr^{-1}, and Asia providing 415. The average annual mean optical depth due to dust at 630 nm is 0.030 ± 0.004.

As Zender et al. (2003) acknowledge, the DEAD model is only of intermediate complexity. One deficiency in the model is a lack of information about the effects of vegetation on emission. Another is the lack of size-dependent energy thresholds for emission during sandblasting. This is because in the saltating flux equation (1.11) the threshold friction speed for saltating particles is assumed to be the minimum threshold friction speed only, at 75 μm, an assumption made because these are the particles most likely to be mobilised and carried in saltation.

1.4.4 Trajectory Simulations

Ellis and Merrill (1995) describe a method for calculating the retrospective back trajectories of dust particles from their deposition points at islands in the Atlantic, such as Barbados. Sal Island in the Cape Verde islands is another useful place for measuring trans-Atlantic dust plumes from the Sahara, due to its close proximity to West Africa, and the large deposition rates onto the islands. Back trajectories have also been used by McKendry et al. (2007) to suggest that the Sahara can be a source of dust for western Canada via Asia and the Pacific. The method involves sampling the dust deposited onto the island, measuring the size and composition of the particles, and the concentration of these. In the published study they investigated the concentrations of aluminium (Al) and used this as the tracer for Saharan, or non-local, mineral dust aerosol.

Back trajectories are calculated using Stokes' law trajectories, which are dependent on the size of the particles: the radii modelled are 1, 2, 3, and 4 μm. Defined is the velocity which balances viscous drag with gravitational settling:

$$w_{\mathrm{s}} = \frac{2r^2 g(d_1 - d_2)}{9\eta} \tag{1.14}$$

The densities of the particle and of the air are d_1 and d_2. Trajectories are calculated on isentropic surfaces, at constant potential temperature θ, and at a time step Δt of 12 hours. These isentropes change with time, carrying the particles with them, and change at a rate w_{i}. The height of the particles at a time t-1 backtracked from a time t is given by:

$$Z^{t-1} = Z^t - (w_{\mathrm{s}} + w_{\mathrm{i}})\Delta t \tag{1.15}$$

The results of this analysis suggest that north Africa was the source for 9% of the measured Al concentration of 2 μm particles in the summer of 1989, compared to 55% of the 4 μm particles. In total, north Africa was identified as the source for 12% of the samples of dust with Al concentrations greater than 1 μg m^{-3}.

Chapter 2

Instruments

2.1 Satellite Instruments

There are a number of satellites currently in orbit carrying instruments with capabilities for remote sensing of aerosols. They achieve this through a variety of methods (eg. forward/nadir views, lidar) and orbits (eg. sun-synchronous, geostationary). Satellite instruments have the advantage of having a large field of view, observing regions hundreds of kilometres across at any moment in time, via remote sensing. They are able to obtain global coverage over a period of days, with one instrument (for a consistent data set).

2.1.1 AATSR

The AATSR (Advanced Along Track Scanning Radiometer) instrument is located on the ESA satellite Envisat. It is a more advanced version of the ATSR-2 instrument on the satellite ERS-2, which itself developed from ATSR-1 on ERS-1. The principal advantage of AATSR over other satellite instruments is that it utilises two views, the forward view and the nadir view, which allows for correction due to the effects of the atmosphere. The forward view retrieves radiance from the atmosphere, whilst the nadir view retrieves radiance from the surface. Its aims are to measure sea surface temperatures (SST) to an accuracy of better than 0.5 K, land surface temperature, vegetation and atmospheric chemistry, as well as aerosol retrieval [envisat.esa.int (last accessed 26/1/07)].

Envisat is in a sun-synchronous polar orbit, at an altitude of 800 km, and an inclination of 98.55 °. The orbital period is 101 minutes, so Envisat orbits just over 14 times per day. The repeat cycle of the nominal orbit is 35 days. AATSR uses 7 channels in the visible and the infrared, at 0.55, 0.66, 0.87, 1.6, 3.7, 11, and 12 μm. The resolution is 1×1 km in the nadir view (555 pixels across the swath), 1.5×1.5 km in the forward view (371 pixels across), and the swath width is 500 km.

The forward view is inclined at an incidence angle (from the nadir) of 55 °, in the direction of ENVISAT's motion. Therefore, it is observing a point over 1000 km ahead of ENVISAT's current position, and it covers this distance in 150 s, when the nadir view observes the point. Figure 2.1 displays the AATSR viewing geometry.

AATSR data files contain several pieces of information relevant to aerosol retrievals. As well as geographical coordinates and time, there are data from each channel for surface albedo, radiances and brightness temperatures. Most useful is the optical depth (at 550 and 660 nm) and the effective radius information, to classify the size of the observed

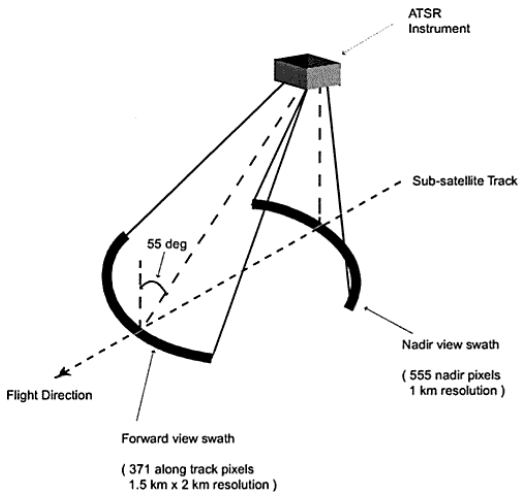

Figure 2.1: AATSR viewing geometry (ESA).

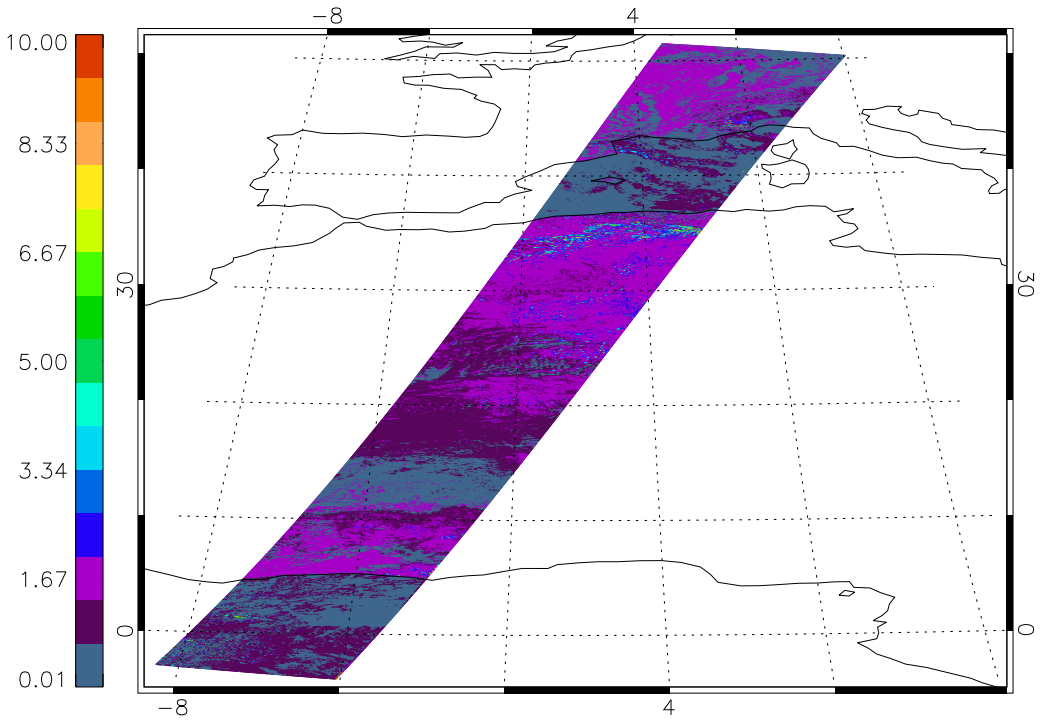

Figure 2.2: Aerosol effective radius (μm) over the Sahara from AATSR data (data courtesy of Andy Sayer, AOPP).

aerosols. The data can be analysed to look specifically for desert (Figure 2.2), maritime, or continental aerosol. For desert aerosols, AATSR generally retrieves effective radius values of between 1-2 μm over the Sahara.

2.1.2 SEVIRI

The SEVIRI (Spinning Enhanced Visible and Infra-Red Imager) instrument is located on the ESA satellite Meteosat 8. Meteosat 8 is part of the Meteosat Second Generation (MSG) project, a series of four satellites to be put into geostationary orbit (altitude 35,600 km) around the Earth. The satellite has been put into orbit at a longitude of 0 °, and at an inclination of 0 °. As well as SEVIRI, Meteosat 8 also carries the Geostationary Earth Radiation Budget instrument (for thermal and reflected solar radiation) and the Search & Rescue Transponder (for distress signals from aircraft, for example).

Meteosat 8's geostationary orbit enables it to take measurements of one particular region of the Earth at all times of the day (except at night), rather than having to wait for the satellite to return from the other side of the orbit. This is especially useful in the case of Saharan dust, since Meteosat 8 is located at longitude 0 °, latitude 0 °, over the Gulf of Guinea. The disadvantage of the geostationary orbit, however, is that SEVIRI's optics require a larger diameter (it has a primary mirror of 0.5 m diameter) to maintain the same resolution as instruments in Low-Earth orbit (LEO), since it is much higher up than LEO satellites (over 40 times higher than AATSR). Obviously, SEVIRI has a better resolution observing at nadir than it does observing towards the limb (the North Atlantic, central Brazil, and Iran mark the edges of the region visible to SEVIRI. All of Africa and most of Europe is visible).

SEVIRI employs 12 channels in the visible and the infrared, at 0.6, 0.8, 1.6, 3.9, 6.2, 7.3, 8.7, 9.7, 10.8, 12, and 13.4 μm, as well as a twelth high-resolution visible (HRV) band [www.eumetsat.int, www.esa.int (last accessed 15/7/07)]. The HRV band has a resolution of 1×1 km, while the other 11 channels have a resolution of 3×3 km. Thus SEVIRI generally has a poorer resolution than most other instruments currently used for aerosol retrieval. Data are taken every 15 minutes.

As with AATSR, SEVIRI data (Figure 2.3) include albedo and radiance information (as well as errors), from which the aerosol optical depth (AOD) can be found. Optical depth information can be distinguished between the various classes of aerosol. To retrieve AOD, data are taken from 8 channels, at 0.6, 0.8, 1.6, 7.3, 8.7, 9.7, 10.8, and 12.0 μm (Brindley and Ignatov, 2006), which then undergo processing (including the removal of data at a solar zenith angle greater than 60 ° or from regions of sun-glint) to retrieve AOD at visible and near-IR channels.

2.1.3 MODIS

The MODIS (MODerate resolution Imaging Spectroradiometer) instrument is located on the NASA satellites TERRA and AQUA [terra.nasa.gov, aqua.nasa.gov (last accessed 1/2/07)]. The two satellites were launched as part of NASA's Earth Observation System (EOS). As well as carrying MODIS and MISR (see below), TERRA carries the instruments ASTER (surface temperatures), CERES (cloud properties and the Earth's radiant system), and MOPITT (pollution in the troposphere). As a satellite, AQUA is principally interested in Earth's water cycle; as well as MODIS, AQUA carries the AIRS and the AMSU (IR and microwave sounders for temperature profiles), the HSB (for humidity

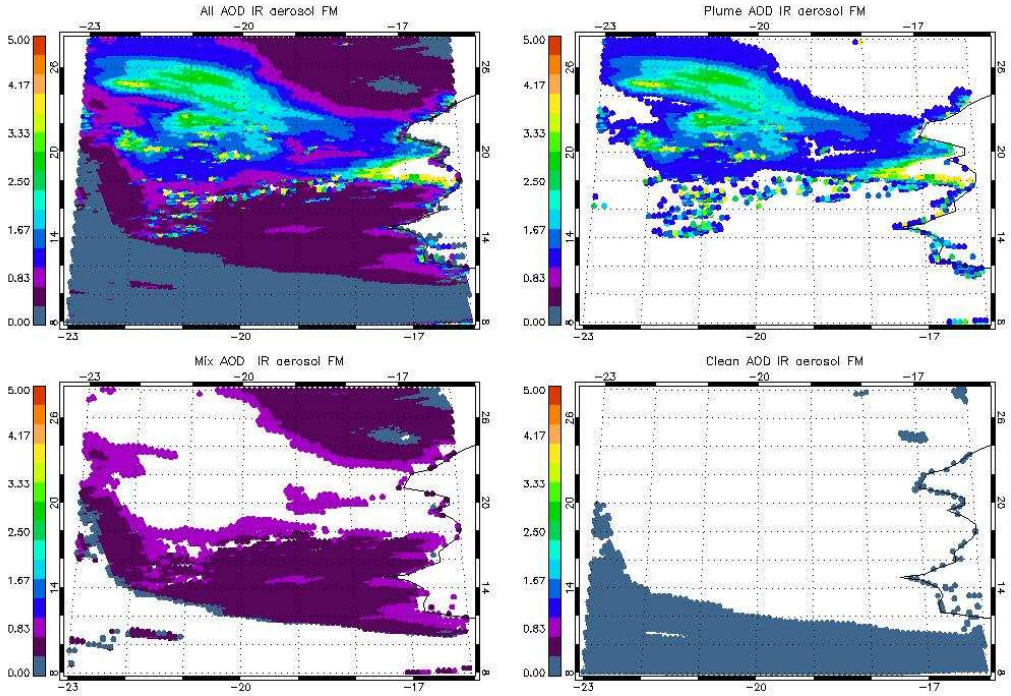

Figure 2.3: Aerosol optical depth in the Atlantic off the coast of west Africa on 8/3/2006 from SEVIRI data, in the infrared. Scale varies between optical depths of 0 and 5. The top left figure shows a plume of Saharan desert dust being swept out over the Atlantic. (Data courtesy of Elisa Carboni, AOPP).

profiles), the AMSR (radiometer for investigating precipitation, SST, snow cover, etc.), and CERES. TERRA and AQUA orbit at an altitude of 705 km, so therefore they have an orbital period of 98.8 minutes, orbiting 14.6 times per day.

MODIS [modis.gsfc.nasa.gov (last accessed 1/2/07)] is designed to investigate numerous properties of the atmosphere, land, and ocean, such as albedo, cloud properties, SST, surface/cloud temperatures, ozone, water vapour and ocean colour, as well as aerosol properties. MODIS operates using 36 channels, in the visible to the infrared (from 405 nm to 14.4 μm). Aerosol boundaries and properties are measured using the first seven channels, using two different algorithms to measure AOD over land and over the ocean: over land, aerosol is measured at 470 and 660 nm (Abdou et al., 2005), while over ocean 550, 660, 860, 1240, 1630 and 2130 nm are used. MODIS' principal advantage over other instruments is its resolution: two of the visible bands have a resolution of 250 m, a further 5 bands have 500 m, while the rest have 1 km. The scanning angle is $\pm 55\,^{\circ}$, so the swath width is 2,330 km. Global coverage is achieved once every one to two days.

2.1.4 MISR

The MISR (Multi-angle Imaging SpectroRadiometer [www-misr.jpl.nasa.gov (last accessed 1/2/07)]) instrument is also located on TERRA. Imaging at four wavelengths (446, 558,

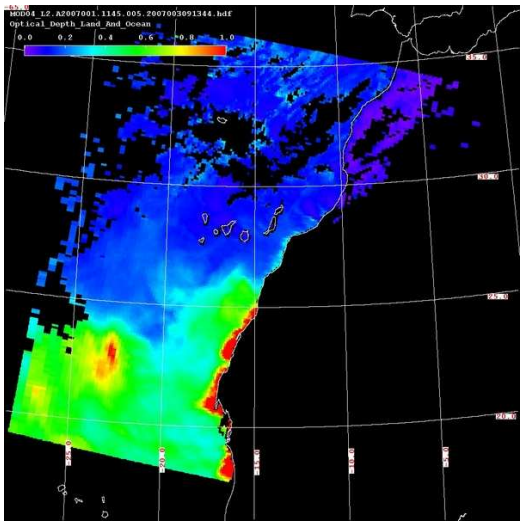

Figure 2.4: Plot of aerosol optical depth, showing dust being blown off west Africa. Image acquired by MODIS on 1/1/07. Image courtesy of NASA (http://ladsweb.nascom.nasa.gov/).

672, and 867 nm), MISR carries nine cameras, each at a fixed angle, such that MISR has a total of 36 channels. There is a camera in the nadir view (0 °), then there are eight cameras at ±26.1 °, ±45.6 °, ±60.0 °, and ±70.5 °, in the forward and aft directions. Each view has specific purposes: nadir is used for precise determination of MISR's geographical location, ±26.1 ° is used for determination of topographic and cloud heights, ±45.6 ° is sensitive to aerosols, ±60.0 ° is used for measurements of albedo, and ±70.5 ° is used to study off-nadir atmospheric effects. The cameras have a maximum resolution of 250 m, though typically the cameras are set to the 'Global Mode', whereby an array of, say, 4×4, pixels is averaged over: this reduces the required data transmission rate.

As with MODIS, aerosol is measured using two different algorithms for over the ocean and over land (Abdou et al., 2005). Over the ocean the 672 and 867 nm bands are used (18 channels), while over land all 36 channels are used.

2.1.5 CALIPSO

The NASA satellite CALIPSO (Cloud-Aerosol Lidar and Infrared Pathfinder Satellite Observation [www-calipso.larc.nasa.gov (last accessed 15/7/07)]) carries the CALIOP (Cloud-Aerosol Lidar with Orthogonal Polarization) instrument. CALIPSO is part of the 'A-Train' of observation satellites, currently consisting of five satellites, maintained in the same orbit as each other, separated only in time. Only 8 minutes separate the time when the first satellite passes over a point and when the last satellite passes. CALIPSO is separated from CloudSat by only 15 seconds. This pattern enables measurements of the evolution of atmospheric conditions (eg. clouds, aerosols) over a short timescale of minutes. CALIPSO is held at an altitude of 705 km, an inclination of 98 °, and an orbital period of 99 minutes.

The CALIOP lidar is designed to study: aerosol and cloud vertical distributions; ex-

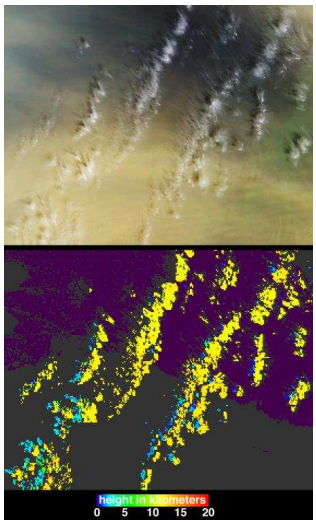

Figure 2.5: Dust storm off west Africa, near the Cape Verde islands. MISR tracks the dust plume's height and motion. The upper image is in the visible, showing cirrus clouds and a layer of dust (in tan). The lower image displays the elevation of the aerosol, the cirrus (yellow) at an altitude of 12 km, while the dust (light blue) is at 2.5 km (the dust aerosol is only picked up due to the contrast with the shadows cast by the cirrus). Image acquired by MISR on 2/3/2003. Image courtesy of NASA (MISR team).

tinction profiles; optical depth; aerosol type; cloud ice and water; cirrus emissivity. It works on the principle of backscattered light (at two wavelengths, 532 nm and 1064 nm) and is polarisation sensitive. There are three receiver channels, one measuring the intensity from the 1064 nm wavelength, and the other two measure the polarised components of the 532 nm wavelength. The output of the CALIOP data is a contour plot (Figure 2.6) of the observed backscatter on a graph of the geographical position of CALIPSO (ie. latitude/longitude) against the altitude of the retrieval. Regions in yellow, orange, red or grey primarily indicate the presence of clouds, but they may also indicate the presence of atmospheric aerosols.

2.1.6 AVHRR

The Advanced Very High Resolution Radiometers (AVHRR) are a series of three instruments flown on American satellites since 1978, and which are able to retrieve aerosols. Their principal objectives are to measure surface temperatures (of the land, oceans, or of cloud tops) and cloud cover, using six channels, from 580 nm to 12.5 μm, at a nadir resolution of 1.09×1.09 km. This enables mapping of day/night cloud and of the surface, detection of land-sea boundaries, snow and ice, and measurements of SST. There are three channels in the IR, which can be used for measuring heat radiation, and so can indicate the presence of aerosols [noaasis.noaa.gov/NOAASIS/ml/avhrr.html (last accessed 19/1/07)].

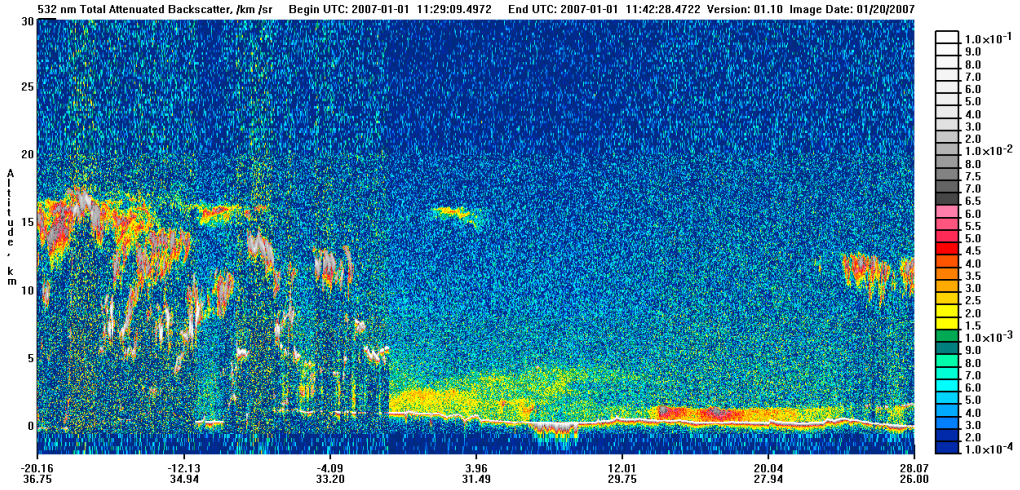

Figure 2.6: CALIPSO data from 1/1/07 (11:28-11:42 UT). The track is heading north from Mozambique to Egypt and Libya. Surface elevation shows up as a red line hovering around the 0 km altitude. Data courtesy of NASA [www-calipso.larc.nasa.gov].

2.2 Surface Projects

Surface projects may not have the global coverage that satellites have, but they are essential for aerosol research. They are needed to characterise surface features such as soil properties, dust particle sizes and classes, and the topography of dust sources. Furthermore, some of the satellites have difficulties resolving aerosol in the lowest kilometre of the troposphere, so that dust sources cannot be precisely identified: while a region can be identified using satellites such as MODIS, it is not clear precisely which surface (dry lake beds, sand dunes, mountains, etc.) within that region produces the atmospheric aerosol.

Surface instruments have a much more accurate spatial resolution than satellite instruments, being in-situ. They also have the advantage of taking direct measurements, rather than carrying out inverse retrieval. On a practical level, they are cheaper to produce, and are easier to maintain than satellites.

2.2.1 AERONET

The AERONET (AErosol RObotic NETwork) is a NASA project within the EOS program (along with the TERRA and AQUA satellites) utilising a ground-based network of photometers to measure solar light intensity, globally distributed (Figure 2.7). It would be preferable for there to be more AERONET sites in some of the larger sources of aerosols (eg. the Sahara), however, it is of course more practical to set up photometers in more heavily populated areas. The network is a standardised system, graded into three levels of quality assurance for each site. The main objective of the project is to take long-term measurements of the optical, microphysical and radiative properties of atmospheric aerosol. Further objectives are to take measurements of solar flux, ocean colour (using

the AERONET-OC network, located on offshore sites, eg. oil platforms), and of water vapour.

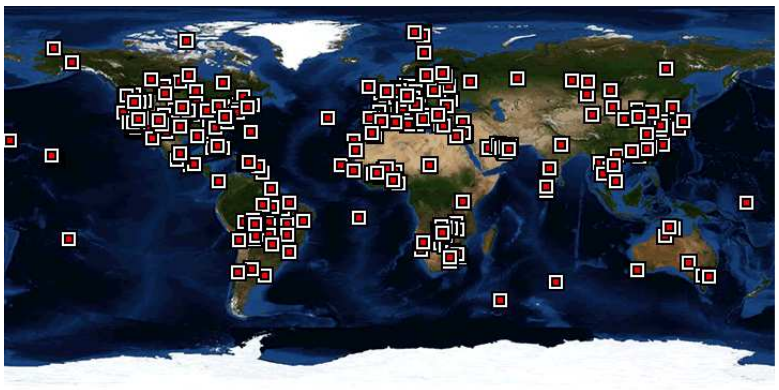

Figure 2.7: Global distribution of AERONET sites (NASA).

Each photometer has eight filters, at 340, 380, 440, 500, 670, 870, 940, and 1020 nm. At each wavelength data are produced for aerosol optical depth/thickness, at various times during the day. AOD is measured by analysing the attenuation of the solar light received by the photometer. Since AOD is measured in just one direction, this is referred to as 'columnar optical depth'.

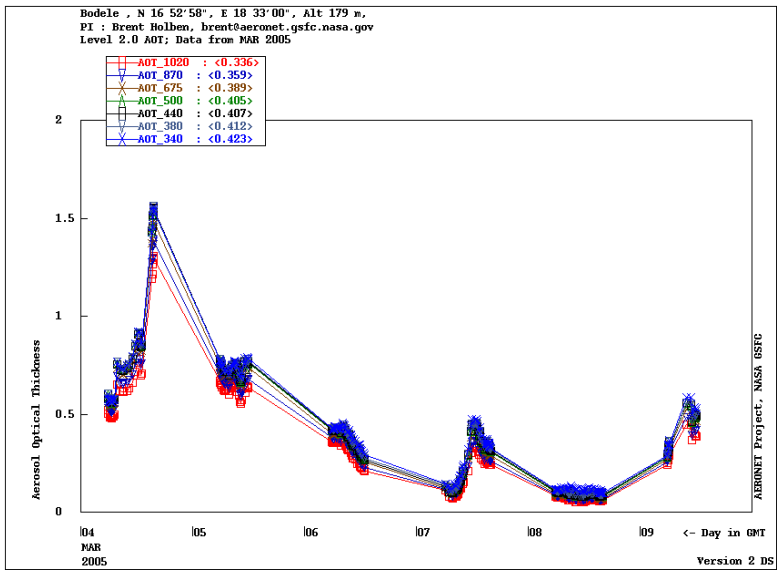

Figure 2.8: AERONET data from the Bodélé site, March 2005. AOD for each wavelength is plotted against time, peaking on the 4th March. Image courtesy of Brent Holben (AERONET).

2.2.2 BoDEx

The BoDEx (Bodélé field experiment) was carried out in February and March 2005 by a team of researchers from the geography departments of Oxford and UCL, and the Direction des Resources en Eau et de la Météorologie, N'Djamena, Chad. The Bodélé depression is located in an exceptionally remote region of north-western Chad between 16-18 °N and 15-19 °E (Prospero et al., 2002), and is the largest single source of tropospheric aerosols in the Sahara.

The BoDEx team used several instruments to measure meteorological conditions, dust storms, and AOD. They used a photometer as part of AERONET (Figure 2.8) for AOD. Automatic weather stations were used to measure temperature, wind velocity, pressure, and solar and UV radiation (Washington et al., 2006a). Vertical wind velocity profiles were measured using Pilot balloon (PIBAL) ascents: nine ascents per day were carried out, at 0000, 0600, 0700, 0830, 1000, 1230, 1500, 1700, and 2100.

Chapter 3

Modelling Dust Transport

3.1 Data Sets

3.1.1 ECMWF meteorological data

The meteorological data set used is the European Centre for Medium-Range Weather Forecasting (ECMWF) Operational Analysis data set, in use since 1994. The data are plotted onto a global $1.125 \times 1.125^\circ$ grid, and, for most of the variables, extended up into the atmosphere on 91 hybrid levels: the data have been on 91 hybrid levels since 0600 on 1/2/2006, they were on 60 levels from 12/10/1999, and on 50 from 1/10/1998. Measurements are made and processed every six hours, at 0000, 0600, 1200, and 1800.

There are wind speeds in three directions: zonal (u), meridional (v), and vertical omega velocity (ω). As with the wind speeds, there is temperature (T) data on all hybrid levels. Log surface pressure ($lnsp$) is plotted on the two-dimensional grid. Finally, each data set is marked with a time (t).

The natural log of the pressure at the surface is defined by $lnsp$, and is used to define the pressure on the hybrid levels. The BADC provides a text file which defines parameters A and B for each hybrid level, which defines the pressure at the edges of each hybrid layer, using:

$$p_{\text{half}} = A + B \exp(lnsp) \tag{3.1}$$

The pressure on each hybrid level i (on which u, v, ω and T are defined) can then be found using:

$$p = \frac{p_{\text{half}}(i) + p_{\text{half}}(i+1)}{2} \tag{3.2}$$

The altitude (z) at each pressure level is defined by reference to T.

Zonal and meridional wind speeds are measured in units of ms^{-1}. The vertical omega wind velocity is measured in units of $\text{Pa}\,\text{s}^{-1}$, which must be converted into units of ms^{-1}, by multiplying by the change in height with respect to pressure.

$$w = \omega \frac{dz}{dp} \tag{3.3}$$

The vertical wind velocity w is in ms^{-1}, ω is in $\text{Pa}\,\text{s}^{-1}$. For use in the model, the hybrid level velocities are interpolated to obtain wind velocity profiles against altitude, in metres.

3.1.2 ISLSCP soil data

The soil data set has been obtained from the International Satellite Land Surface Climatology Project (ISLSCP) via the BADC. It is a global data set, at a resolution of $1\times1\,^\circ$. This is bilinearly interpolated to the coarser resolution ($1.125\times1.125\,^\circ$) of the ECMWF data set.

The soil class is denoted by a soil index value, from 0 to 7. These indices are described in table 3.1. Each class represents the mass fraction of clay, silt, medium/fine sand, and coarse sand present within the soil, and these fractions are taken (with amendments) from table 2 in Tegen et al. (2002). The distributions are normalised so that the total distribution over all particle sizes is 1.

		Percentages			
Soil index	Class	Coarse sand	Medium/fine sand	Silt	Clay
0	Water	-	-	-	-
1	Coarse	44	32	16	8
2	Medium-coarse	10	50	20	20
3	Medium	0	37	33	30
4	Fine-medium	0	27	25	48
5	Fine	0	0	33	67
6	Ice	-	-	-	-
7	Organic	-	-	-	-

Table 3.1: Soil size fractions for each soil class.

For obvious reasons, water, ice and organic (forest, swamp, etc.) are not regarded as a source of dust particles, so they do not have a particle distribution. Coarse sand is defined as particles with radii between 250 and 500 μm, medium/fine sand has radii between 25 and 250 μm, silt has radii between 1 and 25 μm, while clay has radii less than 1 μm. The coarse class (1) fractions have been adjusted from the values provided: Tegen et al. (2002) assume that there is no clay in coarse soil, and so in their usage of the soil textural triangle (which depicts the fractions of clay, silt and sand in coarse, medium, and fine soils) they have added the clay component to the silt component. That there are no particles with radii less than 1 μm appears unphysical, so I present here coarse soil fractions more in keeping with the evidence provided by the soil triangle (from which the size fractions are produced) in figure 3.1.

The particle size distribution ranges from 10^{-2} μm (0.01 μm) to $10^{2.7}$ μm (500 μm). These are spaced by $\delta(\log r)$=0.1.

3.2 Dust Transport

3.2.1 Dust emission

Dust emission is driven by the process of *saltation*, which triggers *sand-blasting*, enabling emission to higher altitudes. Long-distance dust transport relies on the *suspension* of dust particles, generally with a smaller radius. Saltation (Marticorena and Bergametti, 1995) is the motion of a particle which is thrown up into the air through horizontal wind (and the impact of other saltating particles) but which quickly falls back to the ground since the upward velocity is not sufficient to exceed the weight: the maximum height of the

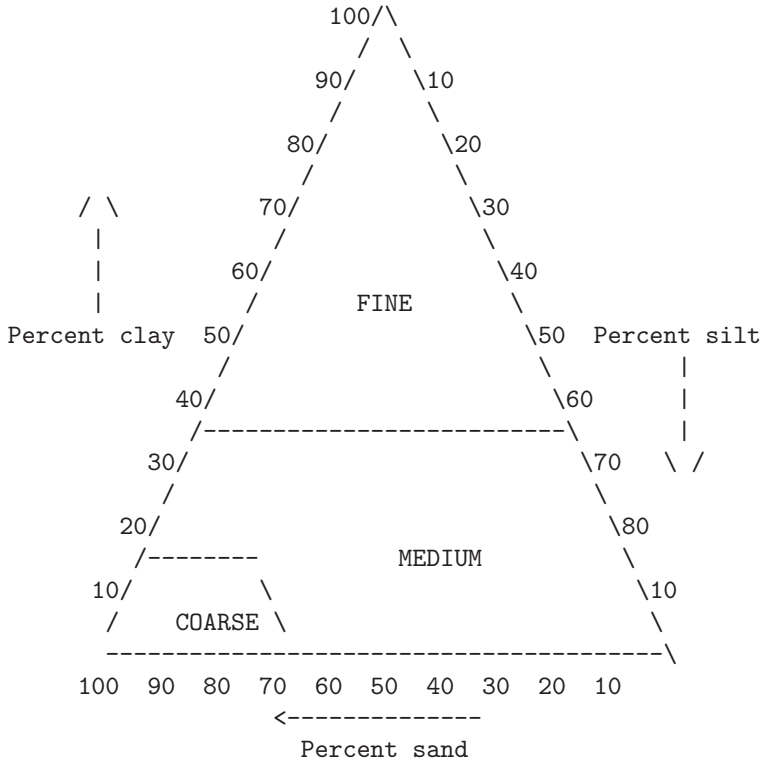

Figure 3.1: Soil triangle, defining soil as fine, medium, or coarse depending on the fraction of clay, silt, or sand within it. Obtained from http://daac.gsfc.nasa.gov/interdisc/readmes/soils.shtml (accessed 13/8/2007). Also available from the BADC at http://badc.nerc.ac.uk/data/islscp/hydro.html ('Global soil properties'- accessed 13/8/2007).

saltation layer is of the order of 1 m. Saltating particles are thrown forward (horizontally) by the wind, and describe a parabolic trajectory. These particles tend to be the larger particles, since these have larger fall velocities than finer particles, with radii greater than 30 μm.

The threshold velocity, u_{tp}, defines the minimum wind velocity required to lift a particle of a certain size up from the surface into the saltation layer, or the velocity at which the aerodynamic forces due to the air equal the particle weight and interparticle cohesion forces (Marticorena and Bergametti, 1995). Marticorena and Bergametti (1995) use a semi-empirical equation to describe it:

$$u_{\mathrm{tp}}(D_{\mathrm{p}}) = \frac{0.129}{\sqrt{1.928(1331 D_{\mathrm{p}}^{1.56} + 0.38)^{0.092} - 1}} \sqrt{\frac{\rho_{\mathrm{p}} g D_{\mathrm{p}}}{\rho_{\mathrm{a}}}} \sqrt{1 + \frac{6 \times 10^{-7}}{\rho_{\mathrm{p}} g D_{\mathrm{p}}^{2.5}}} \tag{3.4}$$

Where D_{p} is the particle diameter, ρ_{p} is the particle density, ρ_{a} is the air density, and g is gravitational acceleration. The minimum threshold velocity occurs at 75 μm in diameter, where the threshold velocity is 0.2 ms^{-1}. Above this diameter, the extra mass in the particle means that gravity holds it down, whereas below this diameter, interparticle

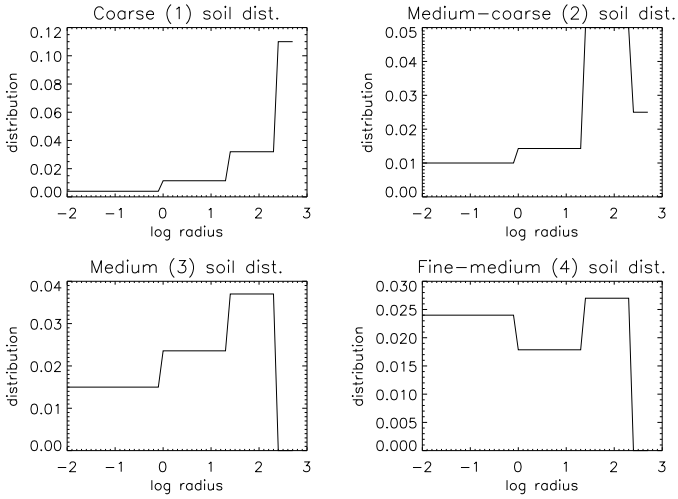

Figure 3.2: Mass distributions of soil classes 1-4. Class 5 (fine) is quite rare in the Sahara region.

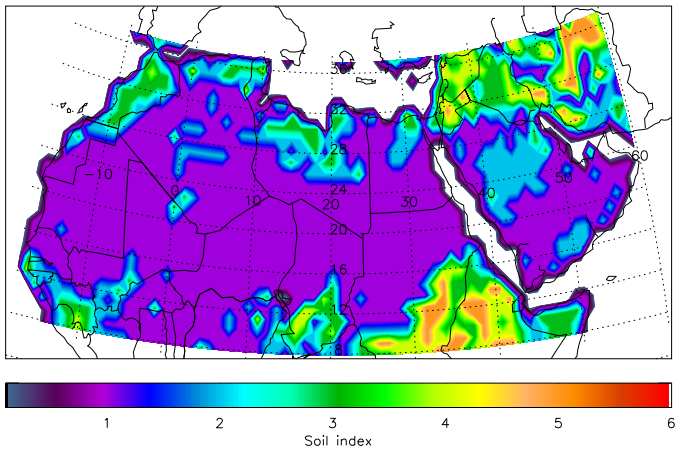

Figure 3.3: Map of soil classes over the Sahara desert region.

cohesion forces bind the particles together more strongly, so that they are less free to move. Figure 3.4 shows how the threshold velocity increases for the smallest particles. These particles are the ones most likely to be suspended in the atmosphere after emission, so it is clear that wind alone cannot mobilise the smallest (sub-micron) particles, which are observed higher in the troposphere, since this requires excessively large surface wind velocities.

When the larger particles strike the surface during saltation, they transfer momentum to the surface particles that they hit. This can break up some of the aggregates in the soil, and encourage the lifting of finer dust particles. Therefore, we can estimate the dust emission flux from the saltation flux: according to Mahowald et al. (2005), since emission requires saltation as an intermediate process, the emission flux is generally regarded as

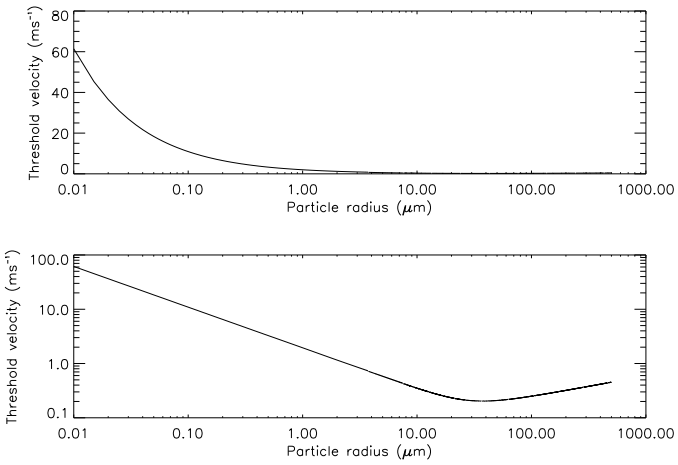

Figure 3.4: Threshold velocity as a function of particle radius. Typical maximum surface wind speed is of the order of 10-20 ms^{-1}. Particles with radii less than 100 nm are often only emitted with difficulty.

being directly proportional to the saltation flux.

Ginoux et al. (2001) provide an empirical formulation to describe this emission flux, which is dependent on wind speeds, particle sizes, and the fraction of each particle size available for lifting. This is the emission flux used in the GOCART model.

$$F_{\mathrm{p}} = \begin{cases} C s_{\mathrm{p}} u_{10\mathrm{m}}^2 (u_{10\mathrm{m}} - u_{\mathrm{tp}}) & \text{if } u_{10\mathrm{m}} > u_{\mathrm{tp}} \\ 0 & \text{otherwise} \end{cases} \tag{3.5}$$

Where C is a factor equal to 1 μg s^2 m^{-5}, s_{p} is the source fraction of each particle size (normalised so that the total source fraction over all size classes is 1), $u_{10\mathrm{m}}$ is the wind speed at 10 m altitude, and u_{tp} is the threshold velocity. The source fraction term is derived from the soil data set described above. Greater surface wind speed has two effects: firstly, it increases the mass from each size class which is lifted; secondly, it reduces the minimum particle size which can be lifted.

A possible extra component to this emission flux has been identified by Kok and Renno (2006). They show that saltating dust clouds produce an electric field (measurements show that this can exceed 100 kVm^{-1}) which produces an extra electric force on the charged dust particles. This force acts upwards, so encouraging emission. They define a 'threshold electric field', similar to the threshold wind velocity, above which the electric force can raise dust particles (though below this the electric field still reduces the required threshold wind velocity):

$$E_{\mathrm{thr}}(d) = 0.69 \sqrt{\frac{\beta}{1.37\pi\epsilon_0 d} + \frac{\rho_{\mathrm{part}} dg}{8.22\epsilon_0}} \tag{3.6}$$

Where d is the particle diameter, β is an empirical constant (10^{-5}-10^{-3} kg s^{-2}), ϵ_0 is the electric permittivity of air, and ρ_{part} is the particle density. However, this effect is still unquantified in terms of emission; it may have a negligible impact, so it will be ignored in the current model.

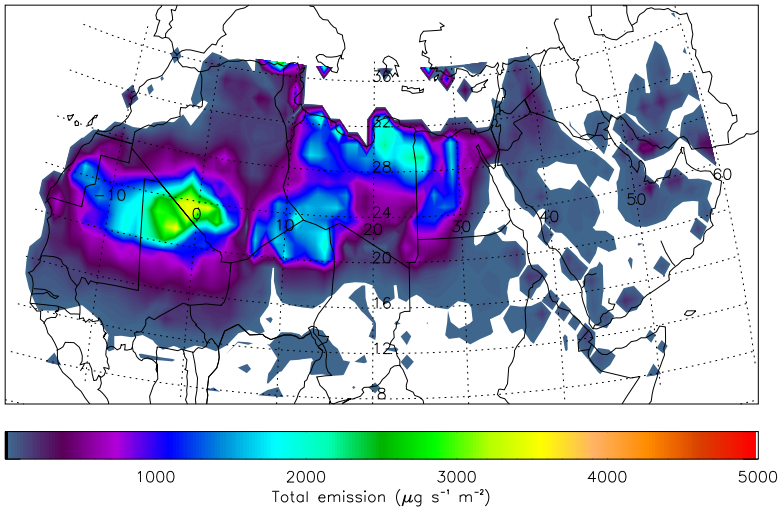

Figure 3.5: Dust emission computed over the Sahara at 12.00 on the 7th March 2006. Note the strong emission coming off southern Algeria, northern Mali, and north-eastern Mauritania, a region previously identified as an important source. This plot is from the period when a very strong dust event, observed by SEVIRI, swept south through West Africa and out into the Atlantic, originating from the lee of the Algerian Atlas mountains (Slingo et al., 2006).

3.2.2 Vertical transport

A flow chart of the vertical transport model can be seen in figure 3.6.

Vertical wind velocity

Vertical wind velocity w is derived from the ECMWF omega velocity, as described above. This is dependent on the height of the level. Physically, w arises from atmospheric *convection*.

The other vertical velocity to account for is the particle fall velocity, which is dependent on particle size and density. This is governed to a good approximation by Stokes' settling, where the settling velocity (Tegen et al., 2002):

$$v_{\text{settling}} = \frac{2r^2 g\rho}{9\eta} C_{\text{Cunn}} \tag{3.7}$$

Where r is the particle radius, g is gravitational acceleration, ρ is the particle density, η is the viscosity of air (or, generally, the viscosity of the fluid through which the particle is falling), and C_{Cunn} is the Cunningham correction factor,

$$C_{\text{Cunn}} = 1 + \frac{\lambda}{r}\left(1.249 + 0.418\exp\left(\frac{-0.847r}{\lambda}\right)\right) \tag{3.8}$$

Where λ is the mean free path of the air molecules, and is small at low altitudes, ie. in the troposphere. Therefore, C_{Cunn} can be taken to equal 1 for tropospheric dust transport.

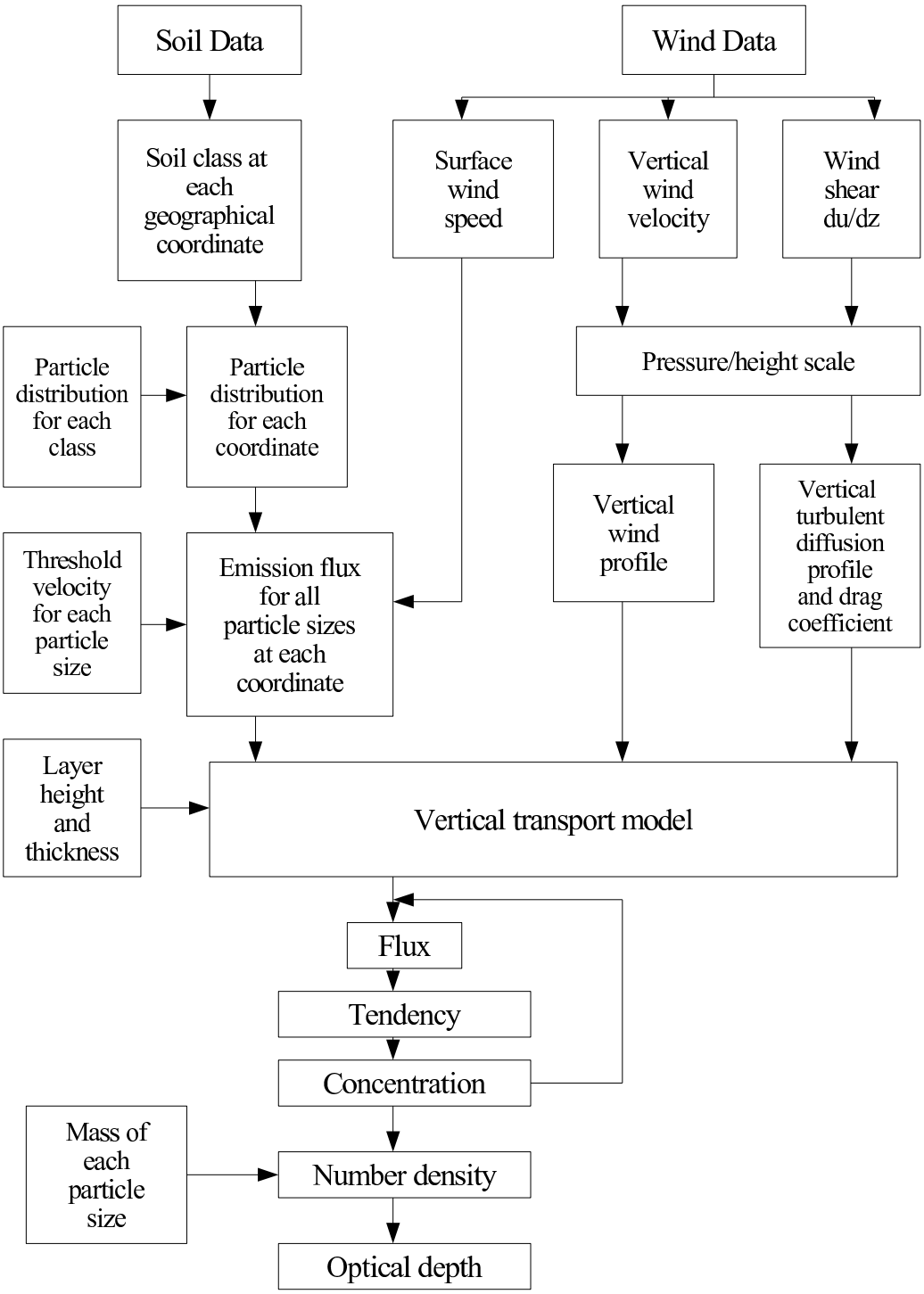

Figure 3.6: Flow chart showing the modules and processes included in the 1D vertical transport model. Fluxes, tendencies, concentrations, and particle sizes are calculated for each particle size and each atmospheric layer/level, for each time step.

These vertical wind velocities contribute the first term in the vertical flux equation. Between layers 1 and 2, the flux is dependent on the concentration of particles between the layers, such that:

$$F_{1:2} = \frac{1}{2}(w - w_{\text{fall}})(\chi_1 + \chi_2) \tag{3.9}$$

Where w is the vertical wind velocity, w_{fall} is the particle fall velocity (settling velocity), and $\chi_{1,2}$ is the concentration in layers 1 and 2. An 'upstream' approximation is used so that if the particles are falling ($w_{\text{fall}} > w$) then the concentration is χ_2, and vice versa.

Vertical turbulent diffusion

Vertical turbulent diffusion is controlled by the vertical turbulent diffusion coefficient, K_{zz}. K_{zz} varies with height within the planetary boundary layer (PBL), above which it is assumed to be a small constant. I use here the scheme described by O'Brien (1970), whereby K_{zz} increases linearly in the constant flux layer, is constant above the PBL, with a polynomial fitted to the region of the PBL above the constant flux layer.

$$K_{zz} = \begin{cases} \kappa u_* z/[1+\phi(z)] & z < z_{\text{B}} \\ K_{\text{A}} + \frac{(z-z_{\text{A}})^2}{\Delta z^2}\Big[K_{\text{B}} - K_{\text{A}} + (z - z_{\text{B}})\big(K'_{\text{B}} + \frac{2(K_{\text{B}}-K_{\text{A}})}{\Delta z}\big)\Big] & z_{\text{B}} < z < z_{\text{A}} \\ \frac{1}{2} & z > z_{\text{A}} \end{cases} \tag{3.10}$$

Where z_{B} is defined as the height of the constant flux layer, the height of which we assume to be of the order of 100 m (Danard, 1981); z_{A} is defined as the height of the PBL, of the order of $u_*/4f$ (Blackadar and Tennekes, 1968) where u_* is the shear velocity (described below) and f is the Coriolis parameter. Δz is the thickness of the PBL above the constant flux layer, z_{A}-z_{B}. $\phi(z)$ is a stability function which we can take to equal zero under adiabatic conditions. K_{A} and K_{B} are the values of K_{zz} at heights z_{A} and z_{B}. In order to determine the profile we must first determine the range of the constant flux layer, which reveals z_{B}, K_{B} and K'_{B}. We know z_{A}, and we can make an approximation for K_{A}, which is identical to the constant and arbitrarily low value of K_{zz} above the height of the PBL. From this information the polynomial can be fitted.

The shear velocity, u_*, arises from the logarithmic horizontal velocity profile, described by Almeida et al. (2006), who define:

$$u = \frac{u_*}{\kappa}\ln(\frac{z}{z_0}) \tag{3.11}$$

Where κ is the von Karman constant ($\kappa = 0.4$), and z_0 is the surface roughness length, a measure of the roughness of the surface. Differentiating with respect to z, we derive an equation that can be used to find u_* from the ECMWF wind velocity profile:

$$u_* = \frac{du}{dz}\kappa z \tag{3.12}$$

The diffusion term in the vertical flux equation is as follows:

$$F_{1:2} = -\frac{K_{zz}}{\delta z}(\chi_1 - \chi_2) \tag{3.13}$$

The thickness of the layer is δz. Therefore the total vertical flux is:

$$F_{1:2} = \begin{cases} (w - w_{\text{fall}})\chi_1 - \frac{K_{zz}}{\delta z}(\chi_2 - \chi_1) & w > w_{\text{fall}} \\ (w - w_{\text{fall}})\chi_2 - \frac{K_{zz}}{\delta z}(\chi_2 - \chi_1) & w < w_{\text{fall}} \end{cases} \tag{3.14}$$

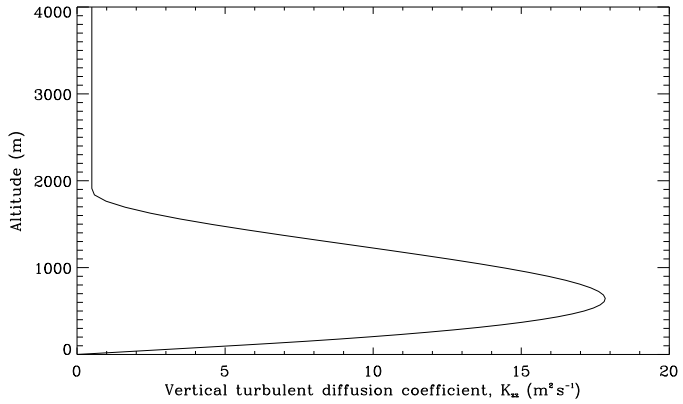

Figure 3.7: An example of the vertical turbulent diffusion coefficient (K_{zz}) profile. Predicted for 38.25 °E, 28.125 °N at 0600 1/2/2006.

The concentration χ_2 is generally less than χ_1, so the diffusion term is generally positive.

To calculate the resultant concentration from the calculated fluxes, we define the *tendency*, $\mathrm{d}\chi_n/\mathrm{dt}$, for the particles to be in layer n during a time interval dt:

$$\frac{d\chi_n}{dt} = \frac{F_{n-1:n} - F_{n:n+1}}{\delta z} \tag{3.15}$$

The tendency is the change in concentration in a layer over a given time interval. To obtain the concentration χ_n we multiply the tendency by the time step dt.

3.2.3 Deposition

Dry deposition

Dry deposition is mainly the result of gravitational settling, though there can also be downdrafts in the vertical wind velocity. Another component of dry deposition is turbulent mixing from the first, or lowest, layer of the atmosphere, down to the surface. Dry deposition is the main mechanism of deposition near the source areas, since the source areas are almost always arid, and forms the bulk of the vertical transport scheme in the model.

Turbulent mixing from the lowest layer to the surface cannot be described using the turbulent diffusion coefficient scheme outlined above, since the surface is not an atmospheric layer, and cannot have a concentration of particles within it. Instead we consider the effect of drag on the lowest layer. Bagnold (1941) (p.51), in his seminal work, defines the drag (stress), τ (kg m^{-1} s^{-2}), which is dependent on the shear velocity u_* and the air density ρ:

$$\tau = \rho u_*^2 \tag{3.16}$$

The drag coefficient (Brown, 1974) (p.50), C_{D}, is defined as the ratio of the drag stress τ and the pressure exerted by the wind velocity:

$$C_{\mathrm{D}} = \frac{\tau}{\rho u^2} \tag{3.17}$$

In the dry case, we can take the turbulent mixing velocity, v_{d} (Tegen and Fung, 1994), out of the first layer to the surface to be:

$$v_{\mathrm{d}} = uC_{\mathrm{D}} \tag{3.18}$$

We then multiply this by the concentration in the lowest layer to find the flux to the surface due to turbulent settling.

Wet deposition

Wet deposition is a rarer process over desert regions, but becomes more relevant for dust plumes that pass over seas and oceans, and other less arid regions, such as Europe. When rain falls through a dust cloud, the process of *scavenging* (Zender et al., 2003) occurs, whereby dust particles are collected within the raindrops and dropped to the surface. This is the dominant deposition process for small particles because dry deposition processes are very inefficient for $D < 2\mu$m, due to very slow particle settling velocities. The larger particles are more likely to have been already removed from the plume by the time the plume reaches an area where precipitation occurs (since source regions are generally arid), so wet deposition is most important for smaller particles, and will occur some distance from the source.

As yet, wet deposition is unaccounted for in the model, due to the fact that the interaction of dust with rain and with clouds is poorly understood, and there is a lack of cloud microphysical measurements in dust regions (Mahowald et al., 2005). Also, precipitation can be highly localised, within the scale of the model grid, which causes the aerosol removal to be highly parameterised. Various modellers have tried to take into account scavenging, such as Tegen and Fung (1994), who define a scavenging ratio, Z, which is the ratio of the concentration of rain in the air to the concentration of aerosol in the air, which is set to be constant. Increasing Z decreases the lifetime of the aerosol particles. This scheme has not been used in the current model, due to a lack of precipitation data.

3.2.4 Results from the 1D vertical transport model

Initially, the model was developed as a 1D column, with dust being distributed vertically. Output are fluxes, concentrations (χ) in each layer for each particle size, and number densities.

Figure 3.8 shows the results from a 27 hour run of the program (with initial conditions set to zero) at a location in north-west Saudi Arabia (38.25 °E, 28.125 °N), using meteorological data from noon of the 16/5/2006.

The time evolution of the total number density for this day shows an interesting feature start to develop at an altitude of about 4500 m after a period of about 20 hours. Typically, the variation of total number density with height is that number density consistently decreases as altitude increases. Here we find that a layer of dust is starting to accumulate, centred at an altitude of 4500 m, and as it evolves we see that the layer diffuses both upwards and downwards. This feature arises due to the vertical wind velocity profile, which changes from positive to negative at just over 5 km. Below this altitude the wind velocity is always positive, so the dust is pushed upwards, but above this altitude the wind velocity is negative and pushes it downwards: this traps the dust into a layer. It is a few hundred metres below 5000 m due to the gravitational settling term. However, dust

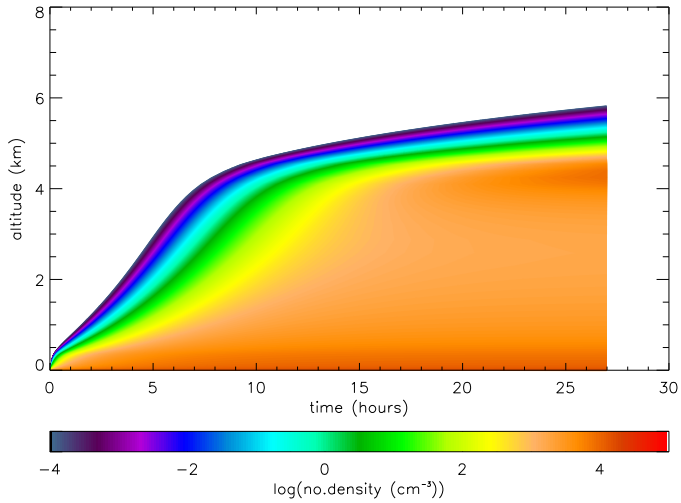

Figure 3.8: 1D model from 38.25 °E, 28.125 °N, on 16/5/2006 at noon. Conditions are kept constant. Shows the time evolution of the total number density of dust particles in each grid square. The time step is 3 minutes.

is able to penetrate the region with negative vertical wind velocity due to the positive (ie. upward) diffusion term.

Figures 3.9a and 3.9b indicate the presence of this layer after 27 hours. Figure 3.9a is a number density plot, and we find that the largest number density is found at around 0.125 μm, compared to the largest concentration in figure 3.9b at around 1 μm. This is due to the emission flux being measured as a mass flux: the concentration of the smaller particles may be less, but each particle carries much less mass than larger particles, since mass goes as r^3, so the number density is correspondingly greater. In figure 3.9a we see that below 0.125 μm the number density drops off sharply, due to the effect of the threshold velocity on the smallest particles. Here the minimum size emitted is 0.1 μm. At other times and locations particles as small as 0.05 μm can be observed in the model: this is due to the surface wind velocities becoming substantial enough to overcome the threshold velocity. Figure 3.9b provides more information as to the 'plume' at 4700 m: the altitude of the plume remains fairly constant for smaller sizes, but for particles reaching 1 μm in radius we see that the altitude of the plume decreases by roughly a hundred metres, due to the fact that these particles require a stronger updraft to hold them at equilibrium against their fall velocities.

The steady-state model is an unphysical simulation of airborne dust, since meteorological conditions are not constant. Figure 3.10 displays the effect of taking into account the changing meteorological conditions: every 6 hours the ECMWF wind fields change, which changes the emission, the vertical wind velocity profiles, and the vertical turbulent diffusion profiles. These have been linearly interpolated to every 20 minutes. Notice how plumes still form, after 1.5 days at about 2 km, after 3 days for the region between 3 and 5 km, and after 5.5 days at 3.5 km. On the sixth day there is a large sand storm near the surface, in the lowest kilometre above the surface, which corresponds to a total optical depth of 7.

In order to find the optimal locations which emit aerosols into the upper troposphere, it is not always useful to use the surface emission contour plots described above. These

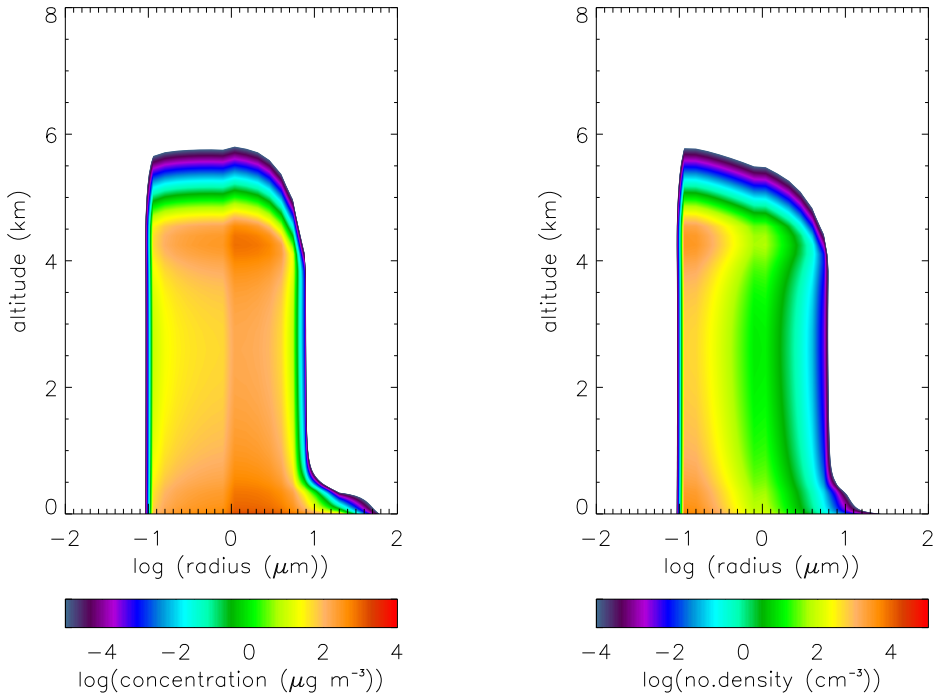

Figure 3.9: (a) Number density in each grid square after 27 hours. (b) Concentration at 27 hours.

plots (of concentration) are biased towards larger particles, which are readily mobilised, but which are extremely unlikely to be transported up above the saltation layer, since they drop out so quickly. This is especially true over the Sahara, where most of the soil is classed as 'coarse', and the fraction of fines is small. Figures 3.11 and 3.12 show the results of a '3D' model, whereby a grid of the 1D columns described above is calculated over the entire Sahara desert region, ie. the 1D model is run simultaneously for all of the locations within the Sahara. From this we can extract and compare the 1D transport for various locations.

3.3 Modelled optical depth

In order to compare the simulated model to reality and to test its validity, it is necessary to extrapolate a property which can be detected. Since it is not possible to measure particle concentrations/number densities directly (ie. in situ), it is necessary to measure radiances (and optical depths) remotely. This is done principally through the use of satellites, though there are ground sites (eg. AERONET) which do this as well. Models such as GOCART and DEAD also calculate optical depth, since the aerosol optical depth can be used to infer the aerosol burden and is generally available as standard from satellite retrievals (Chin et al., 2002).

The optical depth caused by a column of aerosol is dependent on four factors:
(1) The effective refractive index of the mineral (ie. dependent on the dust composition);
(2) The size distribution of the aerosol particles;

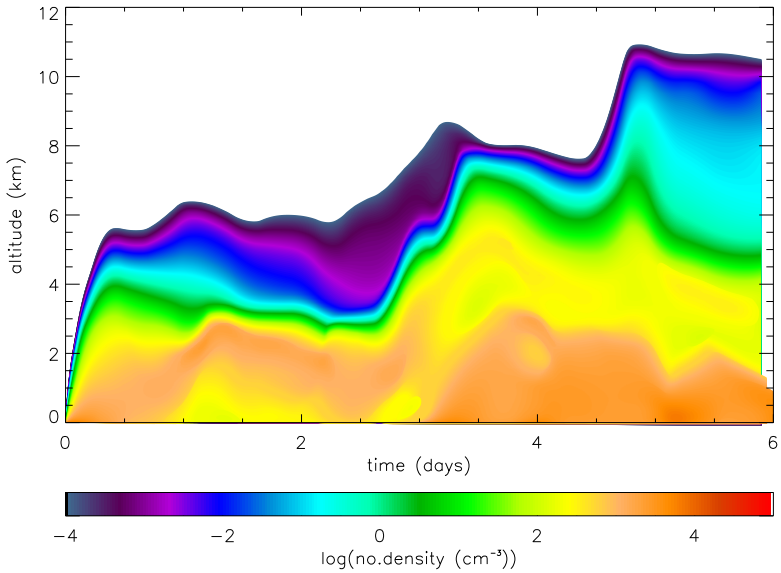

Figure 3.10: The 1D model incorporating varying wind fields, located in north-west Saudi Arabia, at 38.25 °E, 28.125 °N. The model starts at 12.00 on 16/5/2006, and finishes at 12.00 on 22/5/2006.

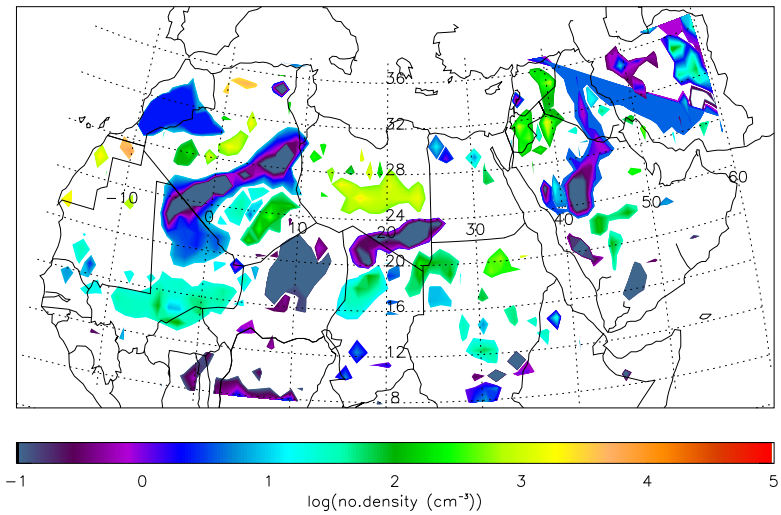

Figure 3.11: Number density in the saltation layer after 20 minutes. Model run on 5/3/2006 at noon.

(3) The depth of the aerosol layer;
(4) The wavelength of the light used to retrieve the aerosol properties.
(2) and (3) are output by the model, while (1) and (4) must be parameterised. The optical depth can be found using Mie scattering theory (Grainger et al., 2004; Lenoble, 1985).

We first define the size (Mie) parameter, dependent on the radius of the particle, r,

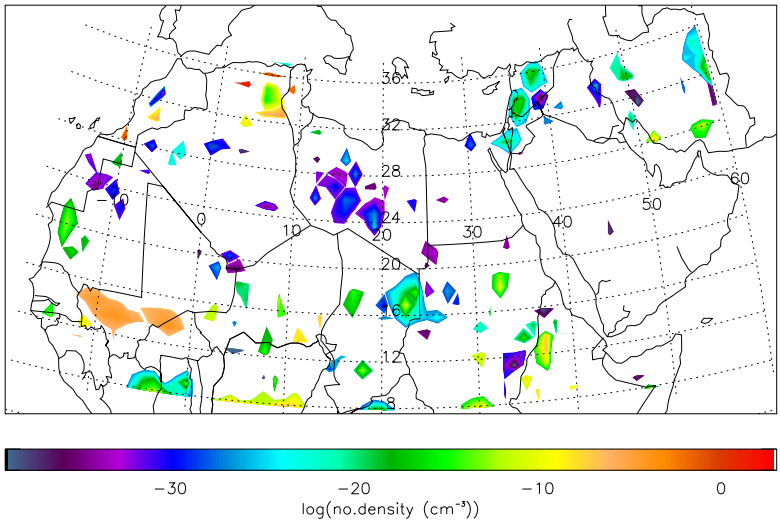

Figure 3.12: Number density at an altitude of 1 km after 20 minutes, at the same time. Note the change in scale.

and the wavelength of the radiation, λ:

$$\alpha = \frac{2\pi r}{\lambda} \tag{3.19}$$

The extinction efficiency, $Q^{\text{ext}}(r)$, is related to the extinction coefficient, $\sigma^{\text{ext}}(r)$, by the cross-sectional area of the particle:

$$\sigma^{\text{ext}}(r) = \pi r^2 Q^{\text{ext}}(r) \tag{3.20}$$

The scattering efficiency is dependent on α, the effective refractive index n, and the coefficients a_{n} and b_{n}, which are the amplitudes of the scattered partial waves:

$$Q^{\text{ext}}(r) = \frac{2}{\alpha^2} \sum_{n=1}^{\infty} (2n+1) Re(a_n^2 + b_n^2) \tag{3.21}$$

For a number size distribution, $n(r)$, the extinction coefficient β^{ext} is given by:

$$\beta^{ext} = \sum \sigma^{\text{ext}}(r) n(r) \tag{3.22}$$

The optical depth, τ, is the integral of the extinction coefficient with the variation in height:

$$\tau = \int_0^{\infty} \beta^{\text{ext}} dz \tag{3.23}$$

The transport model outputs $n(r)$ for each particle size, height layer, and time, and dz for each height layer. An example of the evolution of the modelled optical depth over a particular location along with its associated aerosol distribution is presented in figure 3.13. These results show the limitations of the steady state model, since they suggest that the aerosol optical depth increases almost linearly to a value of around 8.5 after only

27 hours. An aerosol optical depth of 8 is an extremely large value, less than 1 is more usually observed. There are two reasons for this discrepancy: firstly, the steady accumulation of particles in the atmosphere is unphysical; secondly, the optical depth routine includes the number density of particles at the lowest layer, where the largest particles (> 25 μm), with the largest optical depths are allowed to hang in suspension. However, satellites have difficulty observing aerosol in the lowest layers of the atmosphere, so they do not pick up on this contribution to the optical depth.

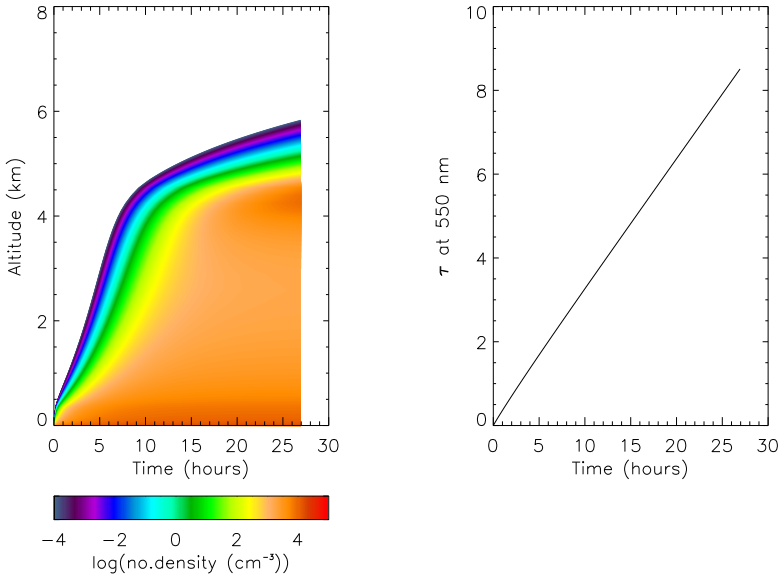

Figure 3.13: An aerosol distribution and the resultant optical depth, from 12.00 of 16/5/2006, at 38.25 °E, 28.125 °N. The optical depth is at a wavelength of 550 nm, and the effective refractive index of the aerosol is assumed to be (1.5+0.004i), which is a reasonable estimate of the refractive index of Saharan dust particles (Munoz et al., 2007).

3.3.1 Determining the number of layers to be used in the model

The model uses 88 height layers, of varying thickness, to calculate the vertical concentration/number density profile of the airborne desert dust. The lowest layer, layer 0 (also known as the saltation layer, in which the heaviest particles are generally confined) has a thickness (δz) of 20 m. δz increases linearly with height, up to a pre-determined thickness ($\delta z_{\max}$) of 250 m for the top layer, taking the altitude to 8 km. Increasing $\delta z_{\max}$ decreases the number of layers. For the sake of precision we require as large a number of layers as possible, for the sake of computer memory and model speed we require as few layers as possible.

In order to find the optimum number of layers, the minimum number of layers to provide accurate results, the optical depth properties, and height, of a dust plume are compared for different numbers of layers. The results are shown in figure 3.14. The 'true' values should converge for the smallest bin sizes (the largest number of layers), so here we need to compare against 401 layers. The chosen number of layers is 88, corresponding to

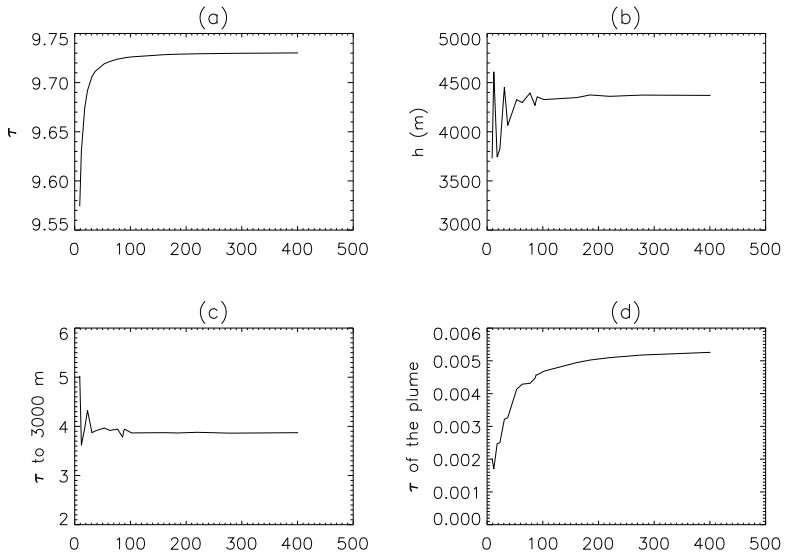

Figure 3.14: Variation of optical/dynamic properties of the aerosol distibution with the number of layers. Values taken from the steady state model from 12.00 on 16/5/2006 at 38.25 °E, 28.125 °N, after 27 hours. (a) Total optical depth. (b) Height of the plume, the layer of maximum number density (above the surface layer). (c) Optical depth down to 3000 m. (d) Optical depth per metre within the plume.

a $\delta z_{\max}$ of 250 m. The optical depth is 9.73022 for 401 layers, and 9.72505 for 88 layers: these agree to 3 significant figures. The average height of the plume is 4370 m for 401 layers, 4320 m for 88 layers: this is 1.2% less than the true value. The optical depth down to 3 km is 3.8719 for 401 layers, 3.9114 for 88 layers: a 1% difference. The optical depth per metre of the densest part of the plume is 0.005259 for 401 layers, 0.004573 for 88 layers, which is 13% less. Below about 88 layers, the values of optical depth and plume height become more erratic and deviate excessively from the true values.

Using this scheme, it is found that a model height of 12 km requires 101 layers, and 110 layers for a height of 16 km.

3.4 The 2D model

Producing a 2D model is a stepping stone to producing a complete 3D model. The 2D model is an extension of the simple 1D model (with varying wind fields interpolated to every 20 minutes), with an extra dimension in the horizontal direction. This dimension has been arbitrarily chosen to be the zonal (x-) direction (the meridional y-direction would work just as well), which requires the zonal wind velocity u for each height layer. The horizontal flux between each x-grid box is dependent on the horizontal wind velocity u and the concentration in each box, which is analogous to equation (3.14).

Preliminary work on the 2D model assumes that the wind across the domain of the model is from a single longitude/latitude coordinate, as in the 1D case. This means that

u, w, and K_{zz} vary only with height, not with x. If the model is run so that all the x-grid boxes at the surface are allowed to emit, then we find that the 2D model reduces to the 1D model. This is because the concentration in each x-grid box at the surface at time $t = 1$ would be identical, therefore the fluxes between each x-grid box at all heights would also be identical. This means that the tendency would be equal to zero, so there would be no horizontal change in concentration. To simulate the effects of preferential source regions, it is possible to set the model so that only specific x-grid boxes are permitted to emit. The evolution of such a scheme is presented in figures 3.15 and 3.16.

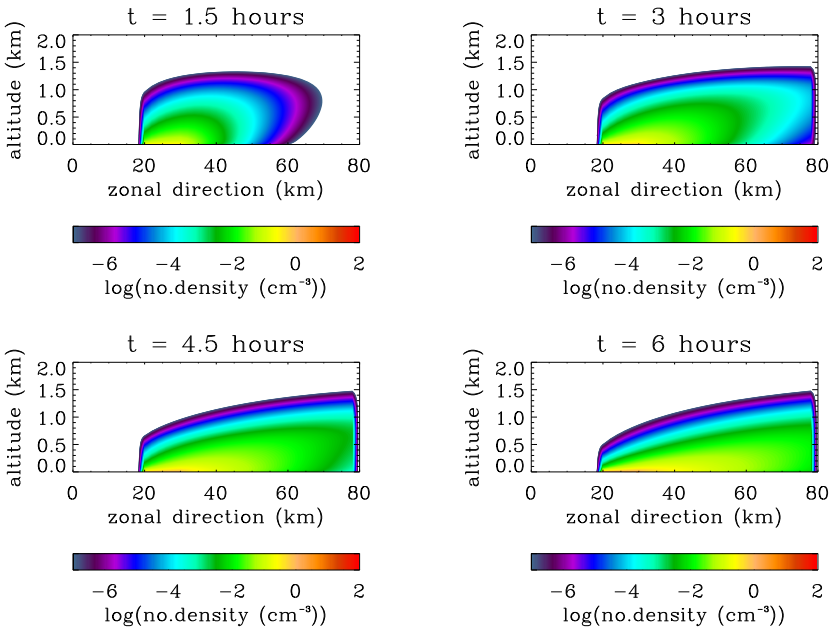

Figure 3.15: Results from the 2D model. Model initialised at 0600 on 1/2/2006 at 38.25 °E, 28.125 °N. Only the strip of land from x = 20 km to x = 30 km is allowed to emit. Evolution is over the first 6 hours.

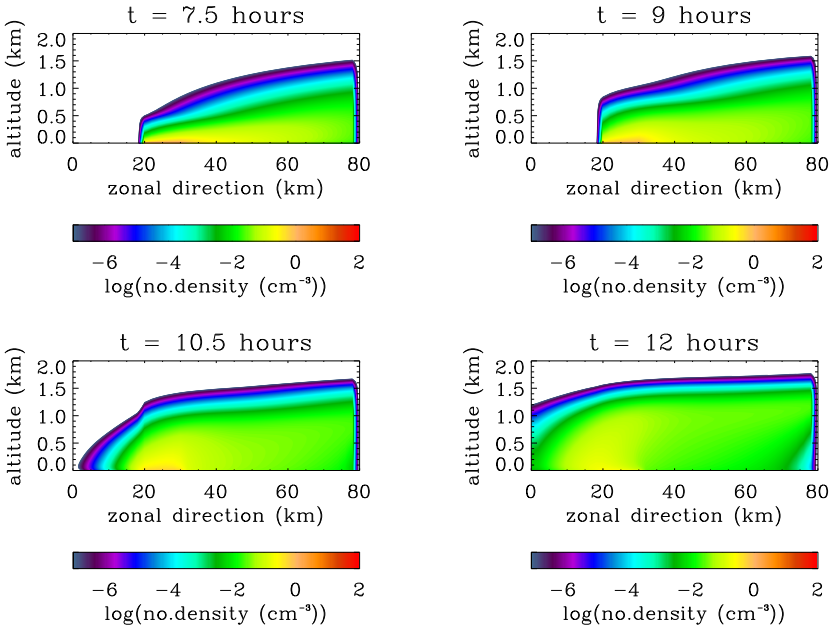

Figure 3.16: Results from the 2D model. Evolution over the second 6 hours. Note the effect of the reversal in the direction of the zonal wind velocity.

Chapter 4

Conclusion

A one-dimensional dust lifting model has been produced, driven by soil and meteorological data. From this, we can calculate the predicted optical depth over a specified geographical coordinate for any date for which we have ECMWF meteorological data.

Output from the model has identified certain regions in the Sahara which are more likely to be sources of mineral dust aerosol, regions which emit aerosol to the upper troposphere. This is often, but not necessarily, related to the total dust emission from the surface.

The model predicts the formation of plumes of dust in the atmosphere, above regions where the vertical wind velocity is positive and below regions where the vertical wind velocity is negative. Plumes may also form in regions where the vertical wind velocity is a local minimum, with higher wind velocities above and below the plume. The conditions under which plumes form are most easily identified through the use of the steady-state model, which keeps the wind conditions constant in time. If the wind conditions are allowed to change, then plumes are seen to evolve not only in thickness, but also in altitude: plumes can ascend or descend depending on the conditions, and on occasion separate plumes can be observed to join up with each other.

The varying wind field model also predicts sand-storm activity, when the concentration of particles within the lowest kilometre of the troposphere is extremely high; the calculated optical depth is correspondingly high.

4.1 Future Work

Future work will have two main aims:
(1) Extension of the model into 3 dimensions.
(2) Comparisons between the model results and satellite observations.

Extension of the model into higher dimensions has first required greater efficiency in the 1 dimensional case, reducing the number of particle sizes, height layers, and increasing the size of each time step. Especially in the case of the grid model (in which the 1D columns were calculated at every location in the Sahara region, including the Middle East: ie. 70 longitude points $\times$ 27 latitude points) the memory requirements can be quite substantial. A compromise is therefore required between model precision and model run-time.

At present, it is envisaged that the 3D model will be regional in scale, and confined

to the Sahara region. Since the model is generalised to any location on the Earth, it will be equally possible to apply the model to other source regions, such as the Taklamakan and the Gobi deserts in China, central Asia, or Australia. These regions can already be studied using the 1D model.

The 3D model will add the effect of horizontal (in the zonal (x) and meridional (y) directions) wind speeds and of horizontal diffusion to the basic 1D model. The width of each grid box (δx and δy) will be of the order of hundreds of metres, or of kilometres. This is due to the fact that horizontal wind speeds are generally at least an order of magnitude greater than the vertical wind speeds. Therefore, in order to satisfy the Courant-Friedrichs-Lewy (CFL) condition (Lin and Rood, 1996),

$$C^x = u\delta t/\delta x \leq 1 \tag{4.1}$$

(where C^x is the CFL number in the zonal direction, u is the zonal wind speed, and δt is the time step; C^y is the CFL number in the meridional direction), we require that the widths δx, δy, be correspondingly larger then the thickness δz. This is required to prevent model instability. This means that the time step and the width of the grid box will depend on the length scale of the processes that are to be studied: for localised processes smaller grid box widths would be required.

More detailed comparisons will also be made with satellite observations, for the purposes of testing the validity of the model. Comparisons will be made with the AATSR and the SEVIRI instruments (described in chapter 2). SEVIRI is particularly useful for this purpose since it is stationed in geostationary orbit above 0 °E, 0 °N, and so has a permanent view of the Sahara region. Meanwhile AATSR can be used due to its superior resolution, and since it looks specifically for desert aerosol as one of its targets.

4.2 Timescale for future progress

It is anticipated that the 3D model will be completed in early 2008. Comparison with satellite observations will be an ongoing process during the DPhil: initial utilisation of AATSR and SEVIRI data should have been carried out by the beginning of 2008 as well. More detailed case studies comparing the 3D model with the observations will be carried out during 2008.

Bibliography

Abdou, W. A., Diner, D. J., Martonchik, J. V., Bruegge, C. J., Kahn, R. A., Gaitley, B. J., and Crean, K. A. (2005). Comparison of coincident Multiangle Imaging Spectroradiometer and Moderate Resolution Imaging Spectroradiometer aerosol optical depths over land and ocean scenes containing Aerosol Robotic Network sites. *Journal of Geophysical Research*, 110(D10S07).

Allen, D. J., Kasibhatla, P., Thompson, A. M., Rood, R. B., Doddridge, B. G., Pickering, K. E., Hudson, R. D., and Lin, S.-J. (1996). Transport-induced interannual variability of carbon monoxide determined using a chemistry and transport model. *Journal of Geophysical Research*, 101(D22):28,655–28,669.

Almeida, M. P., Jr., J. S. A., and Herrmann, H. J. (2006). Aeolian Transport Layer. *Physical Review Letters*, 96(018001).

Bagnold, R. A. (1941). *The Physics of Blown Sand and Desert Dunes*. Methuen, London.

Blackadar, A. K. and Tennekes, H. (1968). Asymptotic Similarity in Neutral Barotropic Planetary Boundary Layers. *Journal of Atmospheric Science*, 25:1015–1020.

Brindley, H. E. and Ignatov, A. (2006). Retrieval of mineral aerosol optical depth and size information from Meteosat Second Generation SEVIRI solar reflectance bands. *Remote Sensing of Environment*, 102:344–363.

Brown, R. A. (1974). *Analytical Methods in Planetary Boundary-Layer Modelling*. Adam Hilger Ltd, 29 King Street, London.

Chin, M., Ginoux, P., Kinne, S., Torres, O., Holben, B. N., Duncan, B. N., Martin, R. V., Logan, J. A., Higurashi, A., and Nakajima, T. (2002). Tropospheric Aerosol Optical Thickness from the GOCART Model and Comparisons with Satellite and Sun Photometer Measurements. *Journal of Atmospheric Science*, 59:461–483.

Chin, M., Rood, R. B., Lin, S.-J., Muller, J.-F., and Thompson, A. M. (2000). Atmospheric sulfur cycle simulated in the global model GOCART: Model description and global properties. *Journal of Geophysical Research*, 105(D20):24,671–24,687.

D'Almeida, G. A. (1986). A Model for Saharan Dust Transport. *Journal of Applied Meteorology*, 25:903–916.

Danard, M. (1981). A Note on estimating the height of the constant flux layer. *Boundary-Layer Meteorology*, 20:397–398.

Ellis, W. G. and Merrill, J. T. (1995). Trajectories for Saharan Dust Transported to Barbados Using Stokes' Law to Describe Gravitational Settling. *Journal of Applied Meteorology*, 34:1716–1726.

Engelstaedter, S., Tegen, I., and Washington, R. (2006). North African dust emissions and transport. *Earth-Science Reviews*, 79:73–100.

Ginoux, P., Chin, M., Tegen, I., Prospero, J. M., Holben, B., Dubovik, O., and Lin, S.-J. (2001). Sources and distributions of dust aerosols simulated with the GOCART model. *Journal of Geophysical Research*, 106(D17):20,255–20,273.

Ginoux, P., Prospero, J. M., Torres, O., and Chin, M. (2004). Long-term simulation of global dust distribution with the GOCART model: correlation with North Atlantic Oscillation. *Environmental Modelling and Software*, 19:113–128.

Ginoux, P. and Torres, O. (2003). Empirical TOMS index for dust aerosol: Applications to model validation and source characterization. *Journal of Geophysical Research*, 108(D17).

Goudie, A. S. and Middleton, N. J. (2006). *Desert Dust in the Global System*. Springer, Heidelburg, Germany.

Grainger, R. G., Lucas, J., Thomas, G. E., and Ewen, G. B. L. (2004). Calculation of Mie Derivatives. *Applied Optics*, 43(28).

Grini, A., Myhre, G., Zender, C. S., and Isaksen, I. S. A. (2005). Model simulation of dust sources and transport in the global atmosphere. *Journal of Geophysical Research*, 110(D02205).

Guerzoni, S., Molinaroli, E., and Chester, R. (1997). Saharan dust inputs to the western Mediterranean sea: depositional patterns, geochemistry and sedimentological implications. *Deep-Sea Research II*, 44(3-4):631–654.

Kaufman, Y. J., Koren, I., Remer, L. A., Tanré, D., Ginoux, P., and Fan, S. (2005). Dust transport and deposition observed from the Terra-Moderate Resolution Imaging Spectroradiometer (MODIS) spacecraft over the Atlantic Ocean. *Journal of Geophysical Research*, 110(D10S12).

Knight, A. W., McTainsh, G. H., and Simpson, R. W. (1995). Sediment loads in an Australian dust storm: implications for present and past dust processes. *Catena*, 24:195–213.

Kok, J. F. and Renno, N. O. (2006). Enhancement of the emission of mineral dust aerosols by electric forces. *Geophysical Research Letters*, 33(L19S10).

Koren, I., Kaufman, Y. J., Washington, R., Todd, M. C., Rudich, Y., Martins, J. V., and Rosenfeld, D. (2006). The Bodélé depression: a single spot in the Sahara that provides most of the dust to the Amazon forest. *Environmental Research Letters*, 1.

Lenoble, J. (1985). *Radiative Transfer in Scattering and Absorbing Atmospheres: Standard Computational Procedures*. A. Deepak Publishing, Hampton, Virginia USA.

Lin, S.-J. and Rood, R. B. (1996). Multidimensional flux-form semi-Lagrangian transport schemes. *Monthly Weather Review*, 124:2046–2070.

Mahowald, N. M., Baker, A. R., Bergametti, G., Brooks, N., Duce, R. A., Jickells, T. D., Kubilay, N., Prospero, J. M., and Tegen, I. (2005). Atmospheric global dust cycle and iron inputs to the ocean. *Global Biogeochemical Cycles*, 19(GB4025).

Marticorena, B. and Bergametti, G. (1995). Modeling the atmospheric dust cycle: 1. Design of a soil-derived dust emission scheme. *Journal of Geophysical Research*, 100(D8):16,415–16,430.

McKendry, I. G., Strawbridge, K. B., O'Neill, N. T., Macdonald, A. M., Liu, P. S. K., Leaitch, W. R., Anlauf, K. G., Jaegle, L., Fairlie, T. D., and Westphal, D. L. (2007). Trans-Pacific transport of Saharan dust to western North America: A case study. *Journal of Geophysical Research*, 112(D01103).

Middleton, N. J. and Goudie, A. S. (2001). Saharan dust: sources and trajectories. *Transactions of the Institute of British Geographers*, NS 26:165–181.

Munoz, O., Volten, H., Hovenier, J. W., Nousiainen, T., Muinonen, K., Guirado, D., Moreno, F., and Waters, L. B. F. M. (2007). Scattering matrix of large Saharan dust particles: Experiments and computations. *Journal of Geophysical Research*, 112(D13215).

O'Brien, J. J. (1970). A Note on the Vertical Structure of the Eddy Exchange Coefficient in the Planetary Boundary Layer. *Journal of Atmospheric Science*, 27:1213–1215.

Prospero, J. M., Ginoux, P., Torres, O., Nicholson, S. E., and Gill, T. E. (2002). Environmental characteristics of global sources of atmospheric soil dust identified with the Nimbus 7 Total Ozone Mapping Spectrometer (TOMS) Absorbing Aerosol Product. *Reviews of Geophysics*, 40(1).

Slingo, A., Ackerman, T. P., Allan, R. P., Kassianov, E. I., McFarlane, S. A., Robinson, G. J., Barnard, J. C., Miller, M. A., Harries, J. E., Russell, J. E., and Dewitte, S. (2006). Observations of the impact of a major Saharan dust storm on the atmospheric radiation balance. *Geophysical Research Letters*, 33(L24817).

Swap, R., Garstang, M., Greco, S., Talbot, R., and Kallberg, P. (1992). Saharan dust in the Amazon Basin. *Tellus*, 44B:133–149.

Tegen, I. and Fung, I. (1994). Modeling of mineral dust in the atmosphere: Sources, transport, and optical thickness. *Journal of Geophysical Research*, 99(D11):22,897–22,914.

Tegen, I. and Fung, I. (1995). Contribution to the atmospheric mineral aerosol load from land surface modification. *Journal of Geophysical Research*, 100(D9):18,707–18,726.

Tegen, I., Harrison, S. P., Kohfeld, K., Prentice, I. C., Coe, M., and Heimann, M. (2002). Impact of vegetation and preferential source areas on global dust aerosol: Results from a model study. *Journal of Geophysical Research*, 107(D21).

Washington, R., Todd, M. C., Engelstaedter, S., Mbainayel, S., and Mitchell, F. (2006a). Dust and the low-level circulation over the Bodélé Depression, Chad: Observations from BoDEx 2005. *Journal of Geophysical Research*, 111(D03201).

Washington, R., Todd, M. C., Lizcano, G., Tegen, I., Flamant, C., Koren, I., Ginoux, P., Engelstaedter, S., Bristow, C. S., Zender, C. S., Goudie, A. S., Warren, A., and Prospero, J. M. (2006b). Links between topography, wind, deflation, lakes and dust: The case of the Bodélé Depression, Chad. *Geophysical Research Letters*, 33(L09401).

Zender, C. S., Bian, H., and Newman, D. (2003). Mineral Dust Entrainment and Deposition (DEAD) model: Description and 1990s dust climatology. *Journal of Geophysical Research*, 108(D14).